



Published in final edited form as:

Neuroimage. 2016 November 15; 142: 260–279. doi:10.1016/j.neuroimage.2016.07.042.

Sheet Probability Index (SPI): Characterizing the geometrical organization of the white matter with diffusion MRI

Chantal M.W. Tax^{a,b,*}, Tom Dela Haije^{c,*}, Andrea Fuster^c, Carl-Fredrik Westin^b, Max A. Viergever^a, Luc Florack^c, and Alexander Leemans^a

^aImage Sciences Institute, University Medical Center Utrecht, Utrecht, Netherlands, Department of Radiology ^bBrigham and Women's Hospital, Harvard Medical School, Boston, MA, United States ^cMathematics and Computer Science, Eindhoven University of Technology, Eindhoven, Netherlands

Abstract

The question whether our brain pathways adhere to a geometric grid structure has been a popular topic of debate in the diffusion imaging and neuroscience society. Wedeen et al. (2012a b) proposed that the brain's white matter is organized like parallel sheets of interwoven pathways. Catani et al. (2012) concluded that this grid pattern is most likely an artifact, resulting from methodological biases that cause the tractography pathways to cross in orthogonal angles. To date, ambiguities in the mathematical conditions for a sheet structure to exist (e.g. its relation to orthogonal angles) combined with the lack of extensive quantitative evidence have prevented wide acceptance of the hypothesis. In this work, we formalize the relevant terminology and recapitulate the condition for a sheet structure to exist. Note that this condition is not related to the presence or absence of orthogonal crossing fibers, and that sheet structure is defined formally as a surface formed by two sets of interwoven pathways intersecting at arbitrary angles within the surface. To quantify the existence of sheet structure, we present a novel framework to compute the sheet probability index (SPI), which reflects the presence of sheet structure in discrete orientation data (e.g. fiber peaks derived from diffusion MRI). With simulation experiments we investigate the effect of spatial resolution, curvature of the fiber pathways, and measurement noise on the ability to detect sheet structure. In real diffusion MRI data experiments we can identify various regions where the data supports sheet structure (high SPI values), but also areas where the data does not support sheet structure (low SPI values) or where no reliable conclusion can be drawn. Several areas with high SPI values were found to be consistent across subjects, across multiple data sets obtained with different scanners, resolutions, and degrees of diffusion weighting, and across various modeling techniques. Under the strong assumption that the diffusion MRI peaks reflect true axons, our results would therefore indicate that pathways do not form sheet structures at every crossing fiber region but instead at well-defined locations in the brain. With this framework, sheet structure location, extent, and orientation could potentially serve as new structural features of brain

*Equal first authors

Publisher's Disclaimer: This is a PDF file of an unedited manuscript that has been accepted for publication. As a service to our customers we are providing this early version of the manuscript. The manuscript will undergo copyediting, typesetting, and review of the resulting proof before it is published in its final citable form. Please note that during the production process errors may be discovered which could affect the content, and all legal disclaimers that apply to the journal pertain.

tissue. The proposed method can be extended to quantify sheet structure in directional data obtained with techniques other than diffusion MRI, which is essential for further validation.

1. Introduction

A three-dimensional Manhattan street grid or the intricate streets of Victorian London, which configuration reflects our brain's organization best? This debate added three Science publications to the list of diffusion MRI (dMRI) literature (Catani et al., 2012; Wedeen et al., 2012a; Wedeen et al., 2012b). Wedeen et al. (2012b) analyzed adjacency and crossings between cerebral fiber pathways of the brain using dMRI and found that the pathways form a 3D grid structure. More specifically, the authors used diffusion spectrum imaging (DSI (Callaghan et al., 1990; Wedeen et al., 2005)), which infers information on the diffusion probability density function (PDF) by extensively sampling q -space in a Cartesian fashion, to reconstruct a so-called path neighborhood with tractography. This path neighborhood can be computed by tracking pathways from a small seed region, and subsequently computing the paths incident on these paths. It was found that the pathways in such a neighborhood cross nearly orthogonally in 2D grid- or sheet-like structures (similar to the “warp and weft of a fabric”) that are layered in 3D space “like pages of a book” (Wedeen et al., 2012a; Wedeen et al., 2012b). This sheet structure was consistently recognized across species and scales, and throughout the white matter.

Catani et al. (2012) suggested that the observed grid pattern is most likely an artifact, attributed to the limitations of DSI used in Wedeen et al. (2012b). The authors showed that diffusion orientation distribution functions (dODFs) as derived from the DSI-PDFs have inherently low angular resolution, and therefore have a limited ability to resolve crossing fibers with small angles. They concluded that this bias towards orthogonal angles negatively impacts the tractography results in Wedeen et al. (2012b) and inadvertently makes “the grid structure of interwoven sheets a very likely configuration” (Catani et al., 2012). By using another dMRI technique called spherical deconvolution (SD) (Dell'Acqua et al., 2007; Dell'Acqua et al., 2010; Tournier et al., 2007), which has a higher angular resolution through the direct reconstruction of the fiber ODF (fODF), they were able to show that non-orthogonal crossings represent a large percentage of the total crossings in white matter (> 88% in a group study of 10 subjects). In addition, Catani et al. noted that the results in Wedeen et al. (2012b) are mainly *qualitative* and that dMRI-based pathways cannot be equated to true axons.

Wedeen et al. (2012a) rebutted the technical concerns regarding DSI and claimed to find further support for the sheet-structure theory in classic degeneration studies. In addition, they agreed that non-orthogonal angle crossings do exist, and stated that Catani et al. did not address the main finding of their study: the existence of sheet structure. This structure “does not depend on fiber orthogonality or the absence thereof” and the authors stated that “there are no mechanisms known whereby technical limitations will create it as an artifact” (Wedeen et al., 2012a).

This debate has gained a lot of attention from the diffusion and neuroscience communities. While still considered controversial by many, the existence of sheet structure could have

significant impact on models of structural and functional brain connectivity, embryogenesis, and development. It could for example play an important role in axonal path-finding during embryogenesis by guiding growing fibers, thereby greatly reducing the complexity of such processes (Wedeen et al., 2012b). The prevalence and geometry of sheet structures in the brain can potentially also be a novel feature to characterize brain structure, complementing the wide range of existing microstructural and geometrical measures (e.g. (Assaf et al., 2008; Astola et al., 2011; Dell’acqua et al., 2013; Fieremans et al., 2011; Leemans et al., 2006; Raffelt et al., 2012; Savadjiev et al., 2012; Tax et al., 2012; Zhang et al., 2012)).

To date, however, there is no general consensus on the degree to which sheet structure is present in the brain. The lack of a clear exposition of the relevant mathematical concepts may have contributed to this ongoing debate. In particular, there still exist ambiguities regarding the exact definition of a sheet structure, the conditions for it to exist, and its relation to orthogonal angles. In addition, the evidence for the existence of sheet structure was mainly *qualitative*, and no extensive *quantitative* analysis was performed so far. In this work, we first formalize the terminology to clarify the definition of sheet structure as proposed by Wedeen et al. (2012b) and the condition for its existence; this is done in Section 2. Subsequently, we propose a robust method to compute a sheet probability index (SPI), which indicates to what extent the data supports a sheet structure, in Section 3.1 and 3.2. An intuitive way to visualize the SPI throughout the brain is described in Section 3.3. We evaluate this method with simulations and real dMRI data sets as described in Sections 3.4 and 4. Finally, we use the proposed method to investigate and discuss some of the claims made in Wedeen et al. (2012a b) and Catani et al. (2012) in Sections 4 and 5. Note that even though we use dMRI data here to investigate the existence of sheet structure, our approach can be extended to compute the SPI in other types of directional data such as polarized-light imaging data (Axer et al., 2001). Preliminary results of this work have been presented at the ISMRM (Tax et al., 2014a) and the BASP workshop (Tax et al., 2015).

2. Theory

In this Section, we present the theoretical background that is required to understand some of the key mathematical concepts in relation to the investigation of the brain’s sheet structure. In Section 2.1, we present a definition of sheet structure in terms of integral curves of vector fields, and in Section 2.2, we discuss the relevant measure used to assess the presence of this sheet structure, i.e. the Lie bracket. In Section 2.3, we explain the Frobenius theorem, which formalizes the necessary and sufficient condition for the sheet structure to exist. Note that we adopt a rather informal mathematical language and omit technical definitions and proofs to make the main concepts accessible to a broader audience. We refer to Appendix A for a list of symbols and Appendix B for a more formal summary.

2.1 Definition of sheet structure

Several definitions and interpretations of ‘sheets’ in the brain exist in the literature (Kindlmann et al., 2007; Schultz et al., 2010; Vilanova et al., 2004; Yushkevich et al., 2008; Zhang et al., 2003). Some major white matter tracts resemble a thin sheet-like structure by itself: well-known examples are the corona radiata and the corpus callosum. Such *single-*

fiber-direction sheets have typically been represented by a sheet-like skeleton (Smith et al., 2006) or a surface (Yushkevich et al., 2008). In contrast, *crossing* or *intertwining-fiber sheets* as proposed by Wedeen et al. (2012b) (hereafter shortened to sheets) are not segregated structures, but are composed of two tracts that cross each other on the same surface in certain regions along their trajectories. As a result, tubular-shaped tracts can in theory still form sheets at locations where they intersect with other structures. Here, we focus on the latter definition of sheet structure and on how such sheets can be detected in directional data where two structures cross.

Consider a set of vectors at each position of the brain $M \subset \mathbb{R}^3$, which can for example be obtained from the dODF or fODF using any dMRI reconstruction technique. With streamline tractography one integrates a smooth three dimensional *vector field* V defined on a subset $N_V \subset M$, generating streamlines (or integral curves) $\Phi^V(s, p)$ ¹ (with s denoting arc length and $p = \Phi^V(0, p)$ the initial spatial position), such that for all $p \in N_V$ the following integrability holds (Fig. 1a):

$$\frac{d}{ds} \Phi^V(s, p) \Big|_{s=0} = V_p. \quad [1]$$

Here, $V_p \in \mathbb{R}^3$ denotes the vector at position p . This idea of integrability can potentially be extended to two vector fields V and W : an integral surface $S \subset N_V \cap N_W$ called the *sheet structure* is defined as the surface S whose tangent plane at p is parallel to the plane spanned by V_p and W_p for all $p \in S$, see Fig. 1b. The requirements for such a surface to exist are formalized in the Frobenius theorem, which states that the vector fields V and W should interact in a ‘nice’ way according to their Lie bracket.

2.2 The Lie bracket

The *Lie bracket*, a mathematical concept from differential topology, is a bilinear operator on two vector fields V and W and defines a third vector field denoted by $[V, W]$. Intuitively, the Lie bracket at a given location p can be understood as the deviation from p when trying to move around in a small loop along the integral curves of V and W with p as the starting position (Fig. 2). Such a loop consists of four ‘legs’ (i.e., a quadrilateral) and starts at point p by following the integral curve $\Phi_s^V(p)$ ² along V for some distance s . After arriving at point $\Phi_s^V(p)$ (the end point of the first leg of the loop), one continues along the vector field W for the same distance s . From the resulting end point of this second leg $\Phi_s^W \circ \Phi_s^V(p)$, where \circ is the symbol used to indicate the concatenation operation, one moves ‘backwards’, along the integral curves of $-V$ and $-W$ in order, again along each leg with the same distance s . The end point of this loop is then written as $\Phi_s^{-W} \circ \Phi_s^{-V} \circ \Phi_s^W \circ \Phi_s^V(p)$ or with the following shorthand notation

¹Here we adopt the flow operator notation Φ^V to represent the streamlines, which has advantages over traditional notation in the remaining Theory sections.

²For notational convenience, we use the flow operator $\Phi_s^V(p) \equiv \Phi^V(s, p)$ if we are considering streamlines of a fixed arc length s .

$$\alpha_p(s) := (\Phi_s^{-W} \circ \Phi_s^{-V} \circ \Phi_s^W \circ \Phi_s^V)(p). \quad [2]$$

In other words, α_p is the curve that comprises the end points of all loops starting in the point p (see Fig. 2a for a schematic overview). For a specific value of s , the difference vector R_p (also called the *closure*) is then defined as

$$R_p(s) := \alpha_p(s) - p. \quad [3]$$

The formal definition of the Lie bracket (Misner et al., 1973; Spivak, 1979) in p , $[V, W]_p$ follows from the Taylor expansion $\alpha_p(s) = \alpha_p(0) + \alpha_p'(0)s + \frac{1}{2}\alpha_p''(0)s^2 + O(s^3)$ (where $\alpha_p(0) = p$ and $\alpha_p'(0) = 0$, and where prime denotes differentiation with respect to s) and taking the limit

$$\lim_{s \rightarrow 0} \frac{R_p(s)}{s^2} = \frac{1}{2}\alpha_p''(0) =: [V, W]_p. \quad [4]$$

See Appendix B for details. At this point we remark that by choosing s sufficiently small, there is a linear relationship between the Lie bracket and the closure (we will use this relation in Section 3.1.3).

2.3 The Frobenius theorem

The requirement for a sheet structure to exist can be understood intuitively by following the line of thinking in the previous section, and is depicted in Fig. 2c and d. The Lie bracket was introduced as the local deviation from p after a small flow over V and W , and if these vector fields are tangent to a sheet in a neighborhood of p then the end point $\alpha_p(s)$ of this flow must lie on the sheet structure as well (Fig. 2c). In the limit of smaller and smaller loop sizes this leads to the Frobenius theorem (Lang, 1995; Spivak, 1979), which tells us that two vector fields V and W form a sheet structure in a neighborhood of point p if and only if the Lie bracket $[V, W]_p$ lies in the plane spanned by V_p and W_p , cf. Fig. 2d. As a comparison, Fig. 2b shows the case (corresponding to Fig. 2a) in which the vector fields V and W do not form a sheet structure.

In practice we can check this condition by examining the component of $[V, W]_p$ normal to V_p and W_p , the *normal component of the Lie bracket* (Wedeen et al., 2012b). We do this by computing the orthogonal projection of the vector $[V, W]_p$ onto the outer product $V_p \times W_p$ (normalized):

$$[V, W]_p^\perp := [V, W]_p \cdot \frac{V_p \times W_p}{\|V_p \times W_p\|}. \quad [5]$$

The sheet structure \mathcal{S} is then given by the set of all points $p \in N_V \cap N_W$ where $[V, W]_p^\perp = 0$. Note that this condition does not involve the presence of orthogonal angles.

3. Materials and methods

We can examine the existence of sheet structure by 1) estimating the integral curves and loops in Eq. [2], 2) estimating the Lie bracket based on Eq. [4], and 3) extracting the normal component of the estimated Lie bracket (Eq. [5]) as an indicator of sheet structure. Note that we can perform these computations for every pair of vector fields in a neighborhood. However, the definitions in Section 2 assume separate, continuous, and smooth unit vector fields, while our input data is a (possibly incomplete) set of unsorted vectors per discrete position, perturbed by noise and generally without consistent sign attributes (e.g. when derived from the dODF or fODF). These issues greatly challenge the actual computation of a Lie bracket.

In Section 3.1 we describe the approach to compute the *discrete* Lie bracket, inspired by the qualitative reconstruction of path neighborhoods in Wedeen et al., 2012a. Our method can deal with noisy vector fields and addresses the problem of sorting vectors in a neighborhood of a point p . In Section 3.2 we further address the issue of noise by deriving a *sheet probability index* (SPI) from multiple computations of the discrete Lie bracket of a pair of vector fields per point. In Section 3.3 we define the *sheet tensor*, which allows us to visualize the Lie bracket for every pair of vector fields. Finally, in Section 3.4 we describe the simulated and acquired MRI data used for the experiments.

3.1 The discrete Lie bracket

We propose here to calculate a discrete Lie bracket by approximating the integral curves in Eq. [2] with tractography (Tax et al., 2015; Tax et al., 2014a; Wedeen et al., 2014), and by computing a large number of loops with configurations as in Fig. 1a. The tractography process and averaging of multiple loop configurations implicitly and partially deals with noise in the Lie bracket computation.

Similar to conventional tractography, we have to make the assertion that each vector is an element of a smooth vector field. Whereas conventional tractography looks for the vector that aligns most with the incoming direction to propagate a tract, here we have to keep track of the whole *frame* of vectors (defined as all vectors at a point) during tracking to be able to switch between different vector fields in a loop. In Section 3.1.1 we describe the clustering of frames (the process of assigning vectors to specific vector fields), which takes care of both the sorting and of possible sign inconsistencies in the vector data. In Section 3.1.2 we outline the *frame tractography* that performs clustering during tract propagation. Finally, the estimation of the Lie bracket is discussed in Section 3.1.3.

3.1.1 Clustering of frames—The purpose of frame clustering is to assign each vector of a frame at a given position to a vector field (Fig. 3). To this end, the frame is compared to an already clustered frame (an ordered set of vectors) at a nearby position. The vectors of the non-clustered frame are matched (permuted) such that the total angle between pairs of vectors is minimized. The frame clustering algorithm can be found in Appendix C1.

3.1.2 Frame tractography—Given a step size h and a discrete distance h (assuming arc length parameterization), we can approximate the flow along a vector field $X \in \{U, V, \dots\}$ with streamline tractography (Mori and van Zijl, 2002). The algorithm explained in Appendix C2 is similar to other deterministic tractography algorithms, but keeps track of the vector fields defined in the neighborhood. Note that we use nearest neighbor interpolation unless stated otherwise. From here on, approximations are marked by a circumflex, i.e., $\hat{\Phi}_h^X$ denotes the approximate flow along X for a distance h , corresponding to the true flow Φ_h^X .

3.1.3 The closure and the Lie bracket—To calculate the discrete Lie bracket we reconstruct approximate flow loops, which can be used to obtain estimates \hat{R}_p of the difference vectors R_p . In practice, we will compute difference vectors for a large number of loops with several configurations (i.e., variations on Eq. [2], see Appendix B). More concretely, given a point p we will consider the set of difference vector estimates $\{\hat{R}_1, \hat{R}_2, \hat{R}_3\}$ resulting from the following loop configurations (Fig. 4):

$$\begin{aligned}\hat{R}_1 &:= \left(\hat{\Phi}_{h_2}^{-W} \circ \hat{\Phi}_{h_1}^{-V} \circ \hat{\Phi}_{h_2}^W \circ \hat{\Phi}_{h_1}^V \right) (p) - p, \\ \hat{R}_2 &:= p - \left(\hat{\Phi}_{h_1}^{-V} \circ \hat{\Phi}_{h_2}^{-W} \circ \hat{\Phi}_{h_1}^V \circ \hat{\Phi}_{h_2}^W \right) (p), \\ \hat{R}_3 &:= \left(\hat{\Phi}_{h_2}^W \circ \hat{\Phi}_{h_1}^V \right) (p) - \left(\hat{\Phi}_{h_1}^V \circ \hat{\Phi}_{h_2}^W \right) (p).\end{aligned}\quad [6]$$

Here, h_1 and h_2 are the flow distances along the integral curves of V and W , respectively. We choose $h_1, h_2 \in \{-h_{max}, -h_{max} + h, -h_{max} + 2h, \dots, -h, h, \dots, h_{max}\}$, where h_{max} is the maximum distance (a parameter in our algorithm). Note that we thus sample all four ‘quadrants’ surrounding point p . The reconstruction of a loop for computation of the difference vector estimate \hat{R}_1 in Eq. [2] (the other difference vectors are computed in a similar manner) is described by the algorithm outlined in Appendix C3.

When all difference vectors are estimated, we can compute an estimate of the Lie bracket $[\widehat{V}, \widehat{W}]_p$ with a simple linear least squares fit corresponding to Eq. [4]

$$\mathbf{R} = \mathbf{H}\boldsymbol{\beta} + \boldsymbol{\epsilon}.\quad [7]$$

Here, \mathbf{R} is a $K \times 3$ matrix with the difference vectors \hat{R} , \mathbf{H} is a $K \times 1$ matrix with the products of the used h_1 and h_2 for the corresponding difference vector, $\boldsymbol{\beta}$ is a 1×3 matrix with the Lie bracket components $[\widehat{V}, \widehat{W}]_p^i$, and $\boldsymbol{\epsilon}$ is a $K \times 3$ matrix with errors, where K is the total number of difference vectors. The errors $\boldsymbol{\epsilon}$ are assumed to be normally distributed. The normal component of the estimated Lie bracket follows from Eq. [5]. In practice, we only compute $[\widehat{V}, \widehat{W}]_p$ when the number of successfully estimated loops and corresponding difference vectors exceeds a minimum threshold.

3.2 Sheet probability index

The algorithm described in Section 3.1 allows us to compute estimates of the Lie bracket normal component $[\widehat{\cdot}, \widehat{\cdot}]^\perp$ for every combination of vectors at every position in the brain, and according to the Frobenius theorem (Section 2.3) a combination of vector fields supports the sheet conjecture if $[\widehat{\cdot}, \widehat{\cdot}]^\perp = 0$. Due to the occurrence of noise, however, the sheet-constraint is rarely exactly fulfilled, and a single estimate does not provide information on its variability. This makes it difficult to quantify to what degree the local structure effectively resembles a sheet.

Ideally, repeated MRI acquisitions could be used to approximate the variance of the estimated Lie bracket normal component. By assuming a normal distribution (in practice verified using a Shapiro-Wilks test) with data-derived mean μ and standard deviation σ , we can calculate the integral probability P_λ inside the region $[-\lambda, \lambda]$ (where we can tune the parameter λ) for the estimated distribution $\mathcal{N}(\mu, \sigma^2)$. P_λ produces a value that lies between 0 and 1 which we coin the *sheet probability index* (SPI) of the local sheet structure. Choosing a higher value for λ means the SPI is less sensitive to small deviations from zero. In practice it is often difficult to acquire a large number of repeated dMRI sets, so we consider residual bootstraps as an alternative (see Section 3.4.2.3).

The introduction of the SPI does not only address the issue of noise, but it also makes the interpretation of the Lie bracket normal component much more intuitive. A high value for the SPI corresponds to a high likelihood of sheet structure ($[\cdot, \cdot]_p^\perp$ is likely close to 0), while a low value indicates that there are significant deviations from sheet structure ($[\cdot, \cdot]_p^\perp$ likely differs significantly from 0).

3.3 Sheet tensors

Investigation of consistent sheet structures in a spatial neighborhood asks for an appropriate way to visualize the SPI throughout the brain. The SPI can be computed for every pair of

vector fields, i.e., n vector fields generate $\binom{n}{2}$ SPI's. In this work we propose to visualize the local sheet structure throughout the brain by means of a *sheet tensor*. Given a pair of vector fields V and W , the sheet tensor at location p is defined as

$$T_p = \frac{P_\lambda}{\beta_1} (V_p \otimes V_p + W_p \otimes W_p) = \frac{P_\lambda}{\beta_1} (V_p V_p^T + W_p W_p^T). \quad [8]$$

Here β_1 denotes the largest eigenvalue of the tensor $(V_p V_p^T + W_p W_p^T)$ and \otimes denotes tensor product. The sheet tensor can then be represented by an ellipsoid whose third eigenvector is normal to the span of V and W , and which defines the color of the ellipsoid in the well-known RGB scheme (normal in left-right direction gives a red tensor, normal in inferior-superior direction gives a blue tensor, and normal in anterior-posterior direction gives a green tensor) (Zhang et al., 2006b). Furthermore, the size of the ellipsoid is determined by

the SPI, where a larger SPI gives larger ellipsoids, and the division by β_1 fixes the largest semi-axis of the ellipsoid for a given SPI. The shape represents the angle between V and W . Fig. 5 shows sheet tensors for different angles and different SPI. The sheet tensor allows us to visualize the SPI for every pair of vector fields at a given location, and can thus also reveal *crossing sheets*.

3.4 Data

We will evaluate our framework with different types of data: analytical vector fields, dMRI simulations, and real dMRI data. These test data sets increase in degree of complexity, allowing us to investigate different aspects of the implemented methodology.

3.4.1 Analytical vector field simulations—We define three vector fields that are tangent to a sphere with radius ρ (U and V are tangent to the upper hemisphere, W is tangent to the lower hemisphere, see Fig. 6a):

$$\begin{aligned} U &= (-\sin\phi_1, \cos\phi_1\cos\theta_2, \cos\phi_1\sin\theta_2), \\ V &= (\cos\phi_2\cos\theta_1, -\sin\phi_2, \cos\phi_2\sin\theta_1), \\ W &= (\cos\phi_2\cos\theta_2, -\sin\phi_2, -\cos\phi_2\sin\theta_2). \end{aligned} \quad [9]$$

Here $\theta_i = \tan^{-1} \frac{x^i}{\sqrt{\rho^2 - (x^1)^2 - (x^2)^2}}$ and $\phi_i = \cos^{-1} \frac{(x^i)}{\rho}$ (with $i = 1, 2$), and $\mathbf{x} = (x_1, x_2, x_3)$ denotes Cartesian coordinates. The integral curves of these vector fields have constant curvature $\kappa = 1/\rho$.

Vector fields U and V form a sheet, so that

$[U, V]_p^\perp = 0 \forall p \in \{\mathbf{x} \in \mathbb{R}^3 | (x^1)^2 + (x^2)^2 < \rho^2, x^3 = z\}$. U and W generally do not form a sheet, and the normal component of the Lie bracket $[U, W]_p$ at $p \in \{\mathbf{x} \in \mathbb{R}^3 | (x^1)^2 + (x^2)^2 < \rho^2, x^3 = 0\}$ is given by

$$[U, W]_p^\perp = \frac{6x^1x^2(-\rho^2 + (x^1)^2 + (x^2)^2)}{\sqrt{(\rho^2 - (x^1)^2)(\rho^2 - (x^2)^2)(\rho^6 - 8\rho^2(x^1)^2(x^2)^2 + 4(x^1)^2(x^2)^2((x^1)^2 + (x^2)^2))}}. \quad [10]$$

A plot of $[U, W]_p^\perp$ as a function of x^1 and ρ is shown in Fig. 6b, where we take $x^2 = -x^1$ so that $[U, W]_p^\perp$ is generally larger than zero. By evaluating Lie bracket estimates along these lines $x^2 = -x^1$ for fixed curvature κ , we can evaluate the performance of the algorithm as a function of the magnitude of the Lie bracket normal component. By varying ρ we can similarly evaluate our Lie bracket estimates as a function of the curvature of the integral curves. Note that these combinations of vector fields generally cross in non-orthogonal angles.

The vector fields are discretized by sampling them on a Cartesian grid with period δ (corresponding to the voxel size). We add noise to the discrete vector fields (N_n noise

iterations) by drawing random samples of a Watson distribution (Chen et al., 2015; Mardia and Jupp, 2009) with probability density function

$$f_W(\pm\tilde{V}_q; V|_q, k) = M\left(\frac{1}{2}, \frac{3}{2}, k\right)^{-1} e^{k(\tilde{V}_q \cdot V_q)^2}. \quad [11]$$

Here, $M\left(\frac{1}{2}, \frac{3}{2}, \cdot\right)^{-1}$ is the Kummer function (Mardia and Jupp, 2009), \tilde{V}_q denotes the perturbed vector at location q , and $k > 0$ is a concentration parameter (here referred to as the ‘SNR level’, higher k results in lower perturbation).

3.4.2 Diffusion MRI data

3.4.2.1 Simulations: dMRI signals were simulated using a ZeppelinStickDot model (Ferizi et al., 2014) with the fiber direction defined by the noise free vector fields described in the previous section. N_n noise iterations were generated using the Rician distribution. We simulate two types of datasets: single shell datasets with 90 directions and $b = 3000 \text{ s/mm}^2$ suitable for SD, and Cartesian sampled datasets with 514 directions (maximum b -value of 10000 s/mm^2) and one $b = 0 \text{ s/mm}^2$ point suitable for DSI (protocol corresponds to the MGH HCP DSI data, see section 3.4.2.2).

3.4.2.2 Real data: We use different dMRI data sets with varying spatial and angular resolutions, diffusion weightings, and sampling schemes to investigate our framework: 1) the $b = 3000 \text{ s/mm}^2$ shell with 90 diffusion directions of three subjects of the WU-Minn Human Connectome Project (HCP) with an isotropic voxel size of 1.25 mm (Glasser et al., 2013; Sotiropoulos et al., 2013; Van Essen et al., 2013); 2) the $b = 3000 \text{ s/mm}^2$ shell with 500 diffusion directions of the MASSIVE database with an isotropic voxel size of 2.5 mm (Froeling et al., 2016); 3) the separate shells ($b = \{1000, 3000, 5000, 10000\} \text{ s/mm}^2$ with $\{64, 64, 128, 256\}$ directions) of one subject of the MGH HCP with an isotropic voxel size of 1.5 mm (Setsompop et al., 2013); and 4) a Cartesian sampled data set (514 directions) with b -values up to 10000 s/mm^2 of the MGH-USC HCP with an isotropic voxel size of 2 mm (<http://www.humanconnectomeproject.org/data/inventory/>).

3.4.2.3 Processing: Data sampled on a single shell was processed using constrained spherical deconvolution (CSD, $I_{max} = 8$) (Tournier et al., 2007) in *ExploreDTI* (Leemans et al., 2009). The response function for the simulated data was generated from the ZeppelinStickDot model, and the response function for real data was computed using recursive calibration (Tax et al., 2014b). Peaks were extracted using a Newton optimization algorithm (Jeurissen et al., 2011) with an fODF peak threshold of 0.1, and a maximum number of 3 peaks. To compute the SPI, we used the N_n noise iterations for simulated data, and generated N_b residual bootstrap realizations for simulated and real dMRI data from a single set of noisy measurements (Jeurissen et al., 2013). The peaks extracted from the different bootstrap realizations were clustered using the method described in Section 3.1.1, taking the peaks extracted from the original data as reference frames.

Cartesian sampled data was analyzed using the DSI model (Wedeen et al., 2005), which was reconstructed with Diffusion ToolKit (DTK) using default settings (Wang et al., 2007). The algorithm readily provides a set of peaks at each position, obtained from the local maxima of a roughly uniform sampling (181 points) of a hemisphere, from which we take at most 3 vectors per position based on the dODF magnitude. No bootstrapping could be performed, so in this case only one Lie bracket was computed for every pair of vector fields.

4. Results

The results for analytical vector field simulations are presented in Section 4.1, for dMRI simulations in Section 4.2, and for real dMRI data in Section 4.3.

4.1 Analytical vector field simulations

With the analytical vector fields we will systematically investigate different aspects of the Lie bracket implementation: the influence of discretization (the finite voxel size δ), the noise (different settings of the concentration parameter k), the curvature κ (by varying ρ), and the Lie bracket magnitude. We use nearest-neighbor interpolation of the vector fields and $N_n = 50$ noise iterations here.

4.1.1 The influence of spatial resolution and noise—Fig. 7 shows results for different voxel sizes $\delta = \{0.5, 1, 2\}$ mm (a–c), different settings for h_{max} (rows) and different SNR levels k (the concentration parameter in Eq. [11], higher k indicates lower perturbation). Here we consider a relatively simple case: since we know which vector belongs to which vector field, we skip the clustering step and show results that are not affected by clustering errors. We set the curvature $\kappa = 1/\rho = 1/26$ mm⁻¹ and estimate the normal component of the Lie bracket at $p = (10, -10, 0)$ to have a Lie bracket magnitude significantly deviating from zero for the given radius ρ .

Each plot shows the mean and range of the estimates $[\widehat{\cdot}, \widehat{\cdot}]_p^\perp$ in the case of sheet (green, $[U, V]_p^\perp = 0$ mm⁻¹) and non-sheet (red, $[U, W]_p^\perp = 0.031$ mm⁻¹). The range becomes smaller with higher k (the noiseless case $k = \infty$ is also plotted) in all cases. The precision of the estimates increases with increasing h_{max} (smaller error bars), and the accuracy increases for $h_{max} = 3$ voxels compared to $h_{max} = 1$ voxel, but remains similar when further increasing to $h_{max} = 5$ voxels. We can see that $h_{max} = 1$ voxel is generally too low to obtain a reasonable accuracy and precision, and to distinguish sheet from non-sheet. The precision is similar for approximately the same h_{max} in mm (see for example the approximately equal error bars in the cases $h_{max} = 3$ voxels, $\delta = 1$ mm and $h_{max} = 5$ voxels, $\delta = 0.5$ mm).

4.1.2 The influence of the Lie bracket normal component magnitude—Fig. 8a shows the mean and range of the estimates $[\widehat{\cdot}, \widehat{\cdot}]_p^\perp$ for different points $p = (x^1, -x^1, 0)$, where the Lie bracket normal component magnitude $[U, W]_p^\perp$ (non-sheet) varies while the curvature remains constant at $\kappa = 1/26$ mm⁻¹. $[U, V]_p^\perp$ (sheet) is evaluated at the same points for reference. We set $k = 350$, $\delta = 1$ mm, and $h_{max} = 5$ voxels. Here and in further analyses, we

apply clustering of the vector fields as described in Section 3.1.1 (using the known vector fields as prior information gave similar results, not shown here).

The estimates $[\widehat{\cdot}, \cdot]_p^\perp$ correspond very well to the true $[\widehat{\cdot}, \cdot]_p^\perp$ for all p in both the sheet and non-sheet case. The range of the estimates remains relatively constant for all cases. The sheet-case can be distinguished from the non-sheet-case for $[U, W]_p^\perp \gtrsim 0.015 \text{ mm}^{-1}$.

4.1.3 The influence of curvature—Fig. 8b shows the mean and range of the estimates $[\widehat{\cdot}, \cdot]_p^\perp$ for different curvatures $\kappa^{-1} = [8, 13, 18, 23, 28, 33]$, where we keep the Lie bracket normal component magnitude $[U, W]_p^\perp$ (non-sheet) constant by evaluating at different points $p = (x^1, -x^1, 0)$ (obtained by solving Eq. [10]). $[U, V]_p^\perp$ (sheet) is evaluated at the same points for reference. We set $k = 350$, $\delta = 1 \text{ mm}$, and $h_{max} = 5 \text{ voxels}$.

The accuracy and precision of the estimates do not seem to depend heavily on the curvature at the considered SNR level and scale, since both the mean and range of the estimates remain relatively constant. We evaluated radii as small as 8 mm , which starts to approximate cortical folding radii. We note here that to detect even smaller radii, a smaller voxel size is required in order to have enough neighborhood information to probe the structure.

4.2 Diffusion MRI simulations

With the diffusion MRI simulations we will investigate more realistic noise scenarios (i.e. we can simulate realistic noise on the actual dMRI images instead of perturbing vectors), the influence of the interpolation technique (nearest neighbor vs fODF interpolation), and the influence of dMRI reconstruction technique (CSD vs DSI). In addition, we will explore the effect of using bootstraps instead of real noise iterations for the calculation of the sheet probability index. We use $N_n = N_b = 50$ noise iterations/bootstrap realizations here.

4.2.1 The influence of noise and interpolation—Here, we extract fODFs and peak directions using CSD from the single shell simulated data. Fig. 9a shows the mean and range of the normal component of the Lie bracket for different settings of h_{max} (rows) and different SNR. We set the curvature $\kappa = 1/\rho = 1/26 \text{ mm}^{-1}$, voxel size $\delta = 1 \text{ mm}$, and evaluate $[\widehat{\cdot}, \cdot]_p^\perp$ at $p = (10, -10, 0)$. We use nearest-neighbor interpolation here, supplemental Fig. S1 shows the same results with linear interpolation on the fODF spherical harmonic coefficients.

Similar to the vector field simulations in Fig. 7, the range of the estimates becomes smaller with higher SNR (the noiseless case is also plotted) and the precision increases with increasing h_{max} . Nearest neighbor interpolation and fODF interpolation give similar results in terms of both the accuracy and precision of the estimates for higher SNR (> 20). We hypothesize that a large number of loops reduces the influence of error propagation along a tract, and ‘smooth out’ some interpolation errors. For an SNR of 10, however, we found that 1 or 2 outliers cause the large range in Fig. 9a at $h_{max} = 3 \text{ voxels}$. This does not occur when using fODF interpolation (Fig. S1), but the mean of the estimates still corresponds very well

to the true value in both cases. For the sake of computational time and cost we use nearest neighbor interpolation in the following.

4.2.2 The influence of dMRI technique: CSD vs DSI—In Fig. 9b, we extracted diffusion ODFs and peak directions using DSI from the Cartesian sampled simulated data. It shows the mean and range of $[\widehat{\cdot}]_p^\perp$ for different settings of h_{max} (rows) and different SNR. We set the curvature $\kappa = 1/\rho = 1/26 \text{ mm}^{-1}$, voxel size $\delta = 1 \text{ mm}$, and evaluate $[\widehat{\cdot}]_p^\perp$ at $p = (10, -10, 0)$.

The mean of the estimates with DSI is in good agreement with the true values. For SNR > 10, the Lie bracket estimates from CSD are more precise than the estimates resulting from DSI (smaller error bars, most obvious at $h_{max} = 3 \text{ voxels}$), even though the simulated CSD datasets have over five times fewer measurements (90 vs 514) and a lower diffusion weighting (maximum $b = 3000 \text{ s/mm}^2$ compared to $b = 10000 \text{ s/mm}^2$).

4.2.3 Sheet probability index—Here, we used the peak directions resulting from CSD on the single shell simulated data. Fig. 10 shows the mean and range of the estimates $[\widehat{\cdot}]_p^\perp$ and the SPI P_λ for different points $p = (x^1, -x^1, 0)$ to vary the Lie bracket normal component magnitude $[U, W]_p^\perp$. $[U, V]_p^\perp$ is evaluated at the same points for reference. We set SNR = 20, $\delta = 1 \text{ mm}$, $\kappa = 1/26 \text{ mm}^{-1}$ and $h_{max} = 5 \text{ voxels}$.

The estimates $[\widehat{\cdot}]_p^\perp$ reflect the true $[\widehat{\cdot}]_p^\perp$ well for all x^1 in both the sheet- and the non-sheet case for the noise iterations. At $x^1 = 11$ the paths start to come in the vicinity of the vector field edge where the vector fields of the non-sheet pair make angles much smaller than the resolving power of CSD, this has a stronger effect on the bootstraps than on the noise iterations (hence the deviation). Overall the bootstraps prove good alternatives to real noise iterations. P_λ decreases in the non-sheet case when the true $[\widehat{\cdot}]_p^\perp$ deviates more from zero.

4.3 Diffusion MRI real data

In this section we present SPI and sheet tensor maps for real diffusion MRI data (we use $N_b = 20$ bootstrap realizations if not mentioned otherwise). In Section 4.3.1 we explain the interpretation of these maps and their relation to the Lie bracket by means of an example data set, and in Section 4.3.2 we investigate inter-subject variability. In the remaining Sections 4.3.3, 4.3.4, and 4.3.5, we consider the influence spatial resolution, diffusion weighting, and dMRI technique, respectively.

4.3.1 Sheet probability index—Fig. 11a (left) shows Lie bracket normal component estimates of the two largest fODF peaks in a single slice of a WU-Minn HCP dataset. An FA color map of the same slice is shown for reference in Fig. 11b. Dark blue areas indicate $[\widehat{\cdot}]_p^\perp \ll 0$, red areas $[\widehat{\cdot}]_p^\perp \gg 0$, and light blue/green/yellow areas $[\widehat{\cdot}]_p^\perp$ close to zero. The order of magnitude of $[\widehat{\cdot}]_p^\perp$ is in agreement with our simulations. Three areas are highlighted with arrows. The areas indicated by the red and green arrow look spatially continuous, whereas the area indicated by the blue arrow looks noisy. The two largest fODF

peaks (used to create this image) in neighboring voxels do not necessarily belong to the same vector fields, we therefore have to consider the Lie bracket normal component for every pair of vector fields in each voxel. This further clarifies our motivation to use sheet tensors for visualization in the following since multiple sheet tensors can be visualized in each voxel. Histograms of the normal component for the bootstraps at these locations are shown in Fig. 11a on the right: high SPI (red arrow, $[\widehat{\cdot}, \widehat{\cdot}]_p^\perp$ concentrated around zero), ‘medium’ SPI (blue arrow, $[\widehat{\cdot}, \widehat{\cdot}]_p^\perp$ spread), and low SPI (green arrow, $[\widehat{\cdot}, \widehat{\cdot}]_p^\perp$ concentrated but not around zero). The histograms illustrate that the normality assumption used to calculate the SPI is reasonable. Figs. 11c and d show SPI maps for the largest fODF peaks.

Fig. 12a shows for one HCP subject sheet tensors on different coronal (top), sagittal (middle), and axial (bottom) slices. Here, $h_{max} = 5 \text{ voxels}$ is used, and sheet tensors with $P_\lambda < 0.2$ are not shown. When navigating through the brain slice-by-slice, these high-sheet probability areas seem to form continuous structures throughout the brain (see Supplementary Video S2). Fig. S3 shows similar results for $h_{max} = 3$, where we can recognize the same sheet areas (sometimes slightly less pronounced). Two high-SPI areas (green rectangle on coronal slice and red rectangle on sagittal slice) are detailed in Figs. 12b and c. The streamlines shown are a subset of the paths reconstructed to compute the Lie

bracket in a voxel in the center of the high-SPI area (the paths $(\widehat{\Phi}_{h_2}^W \circ \widehat{\Phi}_{h_1}^V)(p)$ and $(\widehat{\Phi}_{h_1}^V \circ \widehat{\Phi}_{h_2}^W)(p)$, to be specific). Fig. 12b shows a sheet formed by the corpus callosum (CC) and the corticospinal tract (CST) in the left hemisphere (see also Supplementary Video S4). In addition, the white arrow highlights an area in which *crossing sheets* are found. Fig. 12c shows a more medial and sagittally oriented sheet structure, formed by parts of the CC/CST and anterior-posterior oriented association fibers. Details of a low SPI area (cyan rectangle on axial slice in Fig. 12a) are shown in Fig. 12d. This case highlights an important potential pitfall when using only visual and qualitative analysis to investigate sheet structures: Even though this structure much looks like a sheet from a superior point of view, it is clearly not a sheet from a lateral and posterior point of view (the fibers ‘diverge’ from each other and are not located on a surface, as can be seen in the views (1) and (2)). Our quantitative method indeed finds a low SPI in this area. Several high SPI areas in the brainstem could also be recognized, e.g. on the fourth coronal slice from the left in Fig. 12a.

4.3.2 Inter-subject variability—Fig. 13 shows results for 3 HCP subjects (first three rows, $h_{max} = 5 \text{ voxels} = 6.25 \text{ mm}$) and the MASSIVE dataset (last row, $h_{max} = 2.5 \text{ voxels} = 6.25 \text{ mm}$). For each subject, corresponding coronal, sagittal, and axial slices are shown in the different columns (two different slices per viewpoint). The arrows highlight examples of high-SPI areas that visually appear consistent across subjects.

4.3.3 The effect of spatial resolution—Fig. 13 compares the MASSIVE dataset (2.5 mm isotropic voxels) with the HCP datasets (1.25 mm isotropic voxels), where we kept the maximum distance h_{max} constant at 6.25 mm. In the MASSIVE dataset the same high-SPI areas can be recognized as in the HCP data.

Supplementary Fig. S5 shows results for the same subject as in Fig. 12 (voxel size 1.25 mm, $h_{max} = 5 \text{ voxels} = 6.25 \text{ mm}$) and Fig. S3 (voxel size 1.25 mm, $h_{max} = 3 \text{ voxels} = 3.75 \text{ mm}$), but now we downsampled the data spatially (voxel size 2.5 mm, $h_{max} = 2.5 \text{ voxels} = 6.25 \text{ mm}$). The same sheet structures can still be recognized, but some finer scale structures get lost.

4.3.4 The effect of diffusion weighting—Fig. 14 shows maps of the SPI for different diffusion weightings ($b = \{1000, 3000, 5000, 10000\} \text{ s/mm}^2$) of the MGH HCP data set, where we use CSD to extract the fODF peaks for every shell separately ($h_{max} = 5 \text{ voxels}$). At $b = 1000 \text{ s/mm}^2$ the SPI was significantly lower, which is the direct consequence of the decreased ability to resolve crossing fibers. $b = 10000 \text{ s/mm}^2$ results in the most extensive high-SPI areas, although most of these regions could already be recognized at a b -value of 3000 s/mm^2 .

4.3.5 The effect of dMRI technique: CSD vs DSI—Fig. 15a shows results of a single Lie bracket computation in tissue on the MGH DSI dataset ($h_{max} = 3 \text{ voxels} = 6 \text{ mm}$). Here, we visualize a tensor if $\left|[\hat{\cdot}, \hat{\cdot}]_p^\perp\right| \leq 0.008$ (all tensors have the same size), and we color the voxel red if the minimum $\left|[\hat{\cdot}, \hat{\cdot}]_p^\perp\right|$ in that voxel is larger than 0.025 (which would indicate that there is likely no sheet structure locally, see e.g. Fig. 10). The arrows indicate high-SPI areas that could also be identified in the previous experiments. Many high $\left|[\hat{\cdot}, \hat{\cdot}]_p^\perp\right|$ estimates are found in the gray matter, but the rectangles indicate example areas in the white matter where most likely no sheet exists. The paths in these areas are visualized in Figs. 15b and c.

5. Discussion

The hypothesis that brain pathways cross nearly orthogonally forming two-dimensional sheet-like structures is an active topic of debate (Catani et al., 2012; Wedeen et al., 2012a; Wedeen et al., 2012b). To date, there is no consensus on the large-scale existence of sheet structure, partly because the conditions for sheet structure are unclear (e.g., whether or not it depends on orthogonal angles), and, more importantly, because extensive quantitative proof is still lacking. In this work, we have focused on the definition of sheet structure defined as a surface formed by interwoven pathways, which does not depend on the angle of crossing fibers (see also Fig. S6 for a plot of the angle against the SPI). We have recapitulated the Frobenius theorem and investigated the discrete Lie bracket as a quantitative indicator of sheet structure. We performed extensive validation of the resulting algorithm by quantifying the effects of different settings and parameters. Finally we presented an investigation into the extent of sheet structure presence in the human brain for different spatial resolutions, dMRI models, and other acquisition parameters.

5.1 Sheet or no sheet? Consistency with previous work

The first question that comes to mind is whether we can now prove or disprove the ubiquitous existence of sheet structure in the brain. Our simple simulations show that the discrete Lie bracket can distinguish between *vector fields* that do and do not form a sheet structure (Figs. 7 and 8). Also in the case of *vector fields derived from diffusion MRI*

simulations, the method is able to correctly identify data representing a sheet structure (Figs. 9 and 10). We found that the performance was dependent on factors such as noise, voxel size, curvature, true Lie bracket normal component magnitude, and the chosen dMRI technique, which we discuss in the following sections. To be able to extend the findings from our simulations to the brain, however, we need to make the strong assumption that the vectors (or ODF peak directions) represent true underlying fiber directions, and that tractography correctly reconstructs true underlying bundles. Although these assumptions are often considered to be more or less valid in many connectivity studies, it is well-known that tractography is subject to many limitations and challenges (Jones, 2010), also a concern raised by Catani et al. (2012).

Based on our results from real dMRI data (Figs. 10 – 15), we can only state that the *data supports the existence of sheet structures at several locations in the brain at the investigated scales*, with the SPI indicating the likelihood. Tractography pathways at locations with high SPI values were visually confirmed to form a sheet by reconstructing the path neighborhood as in Wedeen et al. (2012b) (Fig. 12bc). Relying only on visual inspection of (layers of) pathways, however, holds an important pitfall: where paths *seem to form a sheet* from a particular point of view (since a grid pattern is easy to recognize by the human eye), they may not be an actual sheet, which becomes more apparent when the view is rotated (Fig. 12d and 15bc). This discrepancy clearly shows the added value of quantitative analysis in the investigation of such structures in the brain. Whereas Wedeen et al. (2012a b) state that “no brain pathways were observed without sheet structure”, our results indicate that this is not the case: crossing fiber regions with very low SPI could be identified at this scale (Figs. 10–15). At some locations no reliable conclusion can be drawn on the existence of sheet structure for various reasons (e.g. only one fiber population could be reconstructed, the normality condition of the different bootstraps was not fulfilled, or the SPI was not clearly ‘high’ or ‘low’ (Fig. 11c) e.g. due to a high standard deviation in the Lie bracket normal component estimates).

Certain areas with high SPI values were found to be qualitatively consistent across subjects (Fig. 13), indicating that our framework provides reproducible results. In agreement with Wedeen et al. (2012a b), we found high SPI values in crossing regions of the corpus callosum with the cingulum (see supplementary video S2) and SLF 1–3 (e.g. Fig. 12c), and observed the continuous (grid) character of these major longitudinal pathways (as opposed to them being clearly distinct). We also found high SPI values in crossing regions of the corpus callosum and the corticospinal tract (Fig. 12b). The existence of this sheet structure has been much debated, and here we find that the data supports sheet structure at the location where these pathways cross (Wedeen et al., 2012a) with non-orthogonal angles (Catani et al., 2012). However, we did not find a high SPI at crossings between callosal pathways and the fornix due to a high standard deviation of the Lie bracket normal component estimates. We could therefore not draw a reliable conclusion whether or not the data supports sheet structure at this location. Further extensive localization of sheet structures and investigation of the involved pathways is subject to future work.

Is the sheet structure something that can be trivially found in the brain, or is it a ‘special’ configuration? “Wedeen et al. (2015a) remarked that the sheet structure “is mathematically

specific and highly atypical, having prior probability ≈ 0 ”, and that “there are no mechanisms known whereby technical limitations will create it as an artifact”. Indeed, most configurations of vector fields do not form a sheet structure, and in this sense the sheet structure is thus special. On the other hand, one configuration in which two thicker bundles trivially form sheets is when they are both straight. Even though this may approximately occur in some regions (e.g. in the cingulum/corpus callosum), tracts exhibit a significant curvature at the scale we have investigated, and the results we have obtained also show high SPI in regions with high curvature in the streamlines of both vector fields (e.g. Fig. 12b). At this point, we cannot ascribe this phenomenon to a more straightforward alternative geometry.

We did not further investigate the issue of pathways making sharp turns (Wedeen et al., 2012a), which we consider a separate topic; it cannot easily be addressed by current tractography algorithms or by the frame tractography used here because of necessary smoothness constraints.

5.2 The issue of scale

The discrete Lie bracket, and thus the derived SPI and sheet tensor maps, are *locally* defined in terms of the surrounding structure. The term ‘local’ here implies that spatial scale is an important factor in the method. The flow distance h_{max} (that determines the extent to which the neighborhood is taken into account), the voxel size δ , and the curvature of the streamlines affect the performance of the algorithm in different but related ways.

In Fig. 7 we show that for a fixed voxel size and fixed curvature, an increase in h_{max} improves the accuracy and precision of the method. This is likely a result of the corresponding increase of the number of data points in the least squares fit (Eq. [7], where K is determined by h_{max} and the fixed step size $h = \delta/2$). This also motivates the incorporation of multiple loop configurations and the exploration of all four ‘quadrants’ surrounding point p (Sec. 3.1.3). Though increasing h_{max} generally has a positive effect, its value is naturally limited by the domain of definition of the vector fields. If a significant number of the loops extend beyond this domain, the accuracy and precision can be expected to drop. This means we should not choose the value of h_{max} to be much greater than the expected size of the sheet structure, which leads to the interpretation of h_{max} as a *sheet structure scale parameter*: h_{max} serves as an approximate lower bound to the size of the sheet structures that can be detected with the algorithm. Note that taking $h_{max} = 1 \text{ voxel}$ does not lead to reliable estimates of the Lie bracket (Fig. 7), so the voxel size δ is, not unexpectedly, a hard limit on the size of detectable sheet structures. Related to the note that “grid structure was maintained at all scales, from the single voxel, to the lobe, to the hemisphere” (Wedeen et al., 2012b), we can thus conclude that it is only possible to reliably detect sheet structures larger than the voxel scale.

Fig. 7 furthermore shows that the accuracy and precision varies with the voxel size δ and with h_{max} in voxels, but remains relatively constant when h_{max} is defined in millimeters (the product of the former two) at the scales considered. This gives the definition of h_{max} as a sheet structure scale parameter a more intuitive physical interpretation. In our real data experiments, we kept h_{max} constant at 6 – 7 mm. The optimal detection of a given sheet

structure then involves tuning of these parameters: for example smaller or highly curved sheet structures require smaller voxel sizes (to be able to set $h_{max} > 1 \text{ voxel}$) at the cost of a lower precision when keeping h_{max} in voxels constant, or at the cost of higher computational demands when calculating more paths for a higher h_{max} in millimeters. This lower precision at smaller voxel sizes (Fig. 7) occurs because the tractography error *in terms of voxels* remains more or less constant for a given SNR and h_{max} in voxels. Deviations in the Lie bracket, having units mm^{-1} , will thus be larger for a smaller voxel size in terms of millimeters. This implies that the normal component of the Lie bracket should be larger in order to still be able to distinguish sheet from non-sheet for a given SNR and h_{max} in voxels at a smaller voxel size. The physical limits of detecting sheets at particular scales have to be examined further in future work. At the scale investigated in our work, curvature does not have a significant effect (Fig. 8b).

The angle threshold is another parameter that can be varied in our algorithm. In this work, we have set a constant angle threshold of 35 degrees for the whole brain. In tractography, however, a single threshold might not be optimal for all brain pathways and should be adapted to the curvature of the tract relative to the voxel size and the SNR of the data, amongst others (Chamberland et al., 2014). This reasoning can be extended to the frame tractography used in our algorithm: the angle threshold being set too low might result in suboptimal Lie bracket normal component estimates and a failure to detect curved sheets (Fig. S7). Conversely, if the angle threshold is set too high, this might result in tracts taking a wrong turn, outliers, and a lower accuracy and precision.

5.3 The impact of diffusion weighting and dMRI method

The impact of the dMRI method, using DSI versus e.g. SD, has also been a big part of the debate (Catani et al., 2012; Wedeen et al., 2012a). This discussion centers on the ability of these models to accurately resolve the orientations of fiber populations. Although the initial concern was that DSI “does not allow separation of fibers that cross at non-orthogonal angles, thus making a grid structure of interwoven sheets a very likely configuration” (Catani et al., 2012), we find instead that the ability to robustly detect fiber populations mainly influences the precision and accuracy of the Lie bracket estimates (and thus the SPI), but it does not necessarily *promote* sheet structure.

The first factor of importance is the ability to detect *crossing fibers*, since 1) the Lie bracket cannot be computed in voxels with a single fiber population, and 2) paths end prematurely if peaks of a vector field are missing, reducing the number of difference vectors K and thus potentially reducing the accuracy and precision (a similar effect as shown in Fig. 7, where a lower h_{max} in voxels equals a lower amount of reconstructed paths). We visually confirmed that in the DSI experiment (Fig. 15) a lower amount of crossing fibers was detected than in a CSD experiment with similar or lower spatial resolution (e.g. MASSIVE data in Fig. 13), resulting in a lower amount of voxels where the Lie bracket could be computed. This is in agreement with Catani et al. (2012), where it was stated that DSI likely has a lower angular resolution. A second criterion that is of importance here is robustness to noise, or the accuracy and precision of the peak estimates. We investigated this effect using simulated dMRI data (based on the best scoring model of experiments in Ferizi et al., 2014, which also

included high b -values). The results shown in Fig. 9 suggest that the performance of DSI and CSD is comparable for a broad range of SNR with CSD having a higher precision, contradicting the statement in Wedeen et al. (2012a) that “DSI should present the lower risk of bias”.

A comparison between the CSD results of the MASSIVE data with voxel size $\delta = 2.5 \text{ mm}$ (Fig. 13, bottom row) and the MGH DSI data with $\delta = 2 \text{ mm}$ (Fig. 15) reveals similar large scale high-SPI areas. These sheet areas could also be observed in the Wu-Minn HCP subjects (Fig. 13, first three rows). Neither CSD nor DSI results in the detection of sheet structure at *every* crossing fiber location in the brain. Based on our findings, we conclude that DSI has no bias towards detecting sheet structure, and also reveals non-sheet areas (Fig. 15).

A higher diffusion weighting generally causes an increase in the number of voxels with a significantly high SPI value (Fig. 14). Using CSD we find very little high-SPI areas in the $b = 1000 \text{ s/mm}^2$ shell of the MGH HCP data set, while for higher b -values the percentage of voxels that are likely to form sheet structures increases. This is consistent with the fact that the angular resolution increases with higher b -values, confirming the importance of a reasonable “diffusion resolution” (Wedeen et al., 2012a). Increased diffusion weighting, however, also comes at the cost of a lower SNR. Generally, a b -value of 3000 s/mm^2 is used for CSD, and the vast majority of the sheets detected at this b are retained when moving to higher diffusion weighting.

With the ever increasing amount of proposed diffusion models, the reliable extraction of fiber directions is still an active area of research. To assess the presence of sheet structure in dMRI data, one requires a robust and reliable means to determine these peak directions. Our method is general and not limited to a particular dMRI technique or acquisition scheme, and we therefore believe that its performance can be improved with ongoing technical developments in the field.

5.4 Further methodological considerations and potential improvements

The error term ϵ in Eq. [7] includes errors due to the approximation of Eq. [4], and errors in the streamline tractography. The approximation errors depend on h_1 and h_2 and on the underlying vector fields. These errors are small and turn out to be negligible compared to other sources of errors. The tractography errors result from measurement noise, interpolation, curvature of the tracts, and step size h (which is linked to the voxel size in our case), among others. Our experiments indicate that noise has the largest effect; in the case of infinite SNR the estimate is accurate. Regarding interpolation, we opted for simple nearest neighbor interpolation of the vector fields for reasons of speed and computational efficiency (both for DSI and for CSD). In the case of CSD we performed additional experiments using fODF interpolation (strictly speaking the actual diffusion measurements would have to be interpolated), which is more precise (Fig. 9a and Fig. S1) but also more computationally intensive because peak extraction has to be performed at every step. In future work, more advanced tractography algorithms could be used to reconstruct the loops and estimate the Lie bracket (e.g. using more complex integration schemes or combining model fitting and tractography (e.g. (Daducci et al., 2015; Reisert et al., 2014))). The

question of whether the added benefit outweighs the additional computation time (the streamlines computed in the algorithm are fairly short) remains to be answered.

To estimate the Lie bracket and its normal component at point p we reconstruct multiple loop configurations, in all quadrants surrounding point p , and with a range of walking distances. Currently we do a simple linear least squares fit (Eq. [7]) on the difference vectors of these loops. We do not take into account the variance of the measurements or potential outliers that arise, for example, when the tractography takes a wrong path during the reconstruction of a loop. This can potentially be improved by doing a (robust) iteratively weighted least squares fit, with the weight dependent on the variance of the values for a given h_1 h_2 from corresponding loops. In addition, the variance of the difference vectors from single loops potentially holds information on the sheet probability; however, it does not give information on the uncertainty of the underlying peaks.

To compute the SPI maps in the case of CSD we use residual bootstrapping, since the acquisition of repeated dMRI data sets is mostly not feasible. In Fig. 10 we show comparable results between the SPI obtained with residual bootstrapping and the SPI obtained with true noise iterations (in the case of simulations). To the best of our knowledge no bootstrapping method exists for DSI, so the reported DSI results are based on a single noise iteration. This makes the quantification and investigation of sheet structure more difficult since the choice of threshold has a hard effect on the visualization of the sheet tensors, sometimes resulting in regions with noisy (isolated) sheet tensors and high Lie bracket normal components (Fig. 15). This further illustrates the necessity of more extensive evaluation of measurement variance (i.e., the computation of the SPI as opposed to considering only a single measurement) for reliable quantification of sheet structure.

When computation of the SPI was possible (in the case of CSD), we set $\lambda = 0.008$ and we excluded the small percentage of voxels that did not have normally distributed Lie bracket normal components over the bootstrap iterations. In future work, the distribution of normal components per voxel and the optimal way to extract an SPI from this (e.g. detection of outliers, fitting, threshold settings) could be investigated more thoroughly. In this work, the value for λ was chosen based on the variability in simulation experiments, and the used setting resulted in regions of smoothly varying SPI with sheet tensors of a similar orientation (i.e. normal) in a certain neighborhood. This suggests that continuous sheet structures could perhaps be better visualized as actual surfaces; tractography could be extended to sheetography by means of a surface propagation process. There are examples of surface reconstruction approaches for DTI data, e.g. (Vilanova et al., 2004; Zhang et al., 2003), which compute streamsheets at points where the DTI tensor has a high planarity coefficient C_p (Westin et al., 2002). We found points in the data where the SPI and the C_p were both high, and where the reconstructed surfaces corresponded well with the information represented by the sheet tensor. This is however no strict prerequisite for the presence of sheet structure. There are places with a high C_p without sheet structure (i.e., low SPI due to spatial incoherence of the data), and places with a low C_p that do show evidence of sheet structure (i.e., high SPI, for example in the case of several sheet structures crossing in a voxel). A comparison between the SPI and different DTI shape measures is included in the supplementary materials (Fig. S8).

In this manuscript we view the Lie bracket in terms of the integral curves of vector fields (Eq. [4]), which is equivalent to a combination of differential operators on the vector fields known as the commutator (see Eq. [13] in Appendix B for details). This raises the question of whether there might be an alternative way to calculate the Lie bracket that does not require the reconstruction of many loops, which is computationally expensive. A direct discretization of Eq. [13] would involve the computation of vector field derivatives, which is a complicated operation. A finite difference implementation does not give stable results in the case of noise. A very recently proposed method to estimate the Lie bracket for diffeomorphic registration purposes computes central difference Jacobians of discrete vector fields by considering them as bandlimited signals in the Fourier domain (i.e. truncating the high frequency components) (Zhang and Fletcher, 2015). However, in addition to discretization and noise, our application has other major challenges: 1) all peaks in a certain neighborhood would have to be clustered into distinct vector fields to be able to compute the Jacobian; 2) there are potential sign inconsistencies between neighboring peaks; and 3) there is no guarantee that all peaks of a vector field exist in a certain neighborhood. The first two challenges are addressed in our algorithm by clustering the peaks into vector fields ‘on the fly’ during the proposed frame tractography. The third challenge still affects our method: In the case of missing peaks the path is terminated, resulting in fewer difference vectors to compute the Lie bracket. This has an important influence on the precision of the estimates (see e.g. the experiments for different h_{max} in Fig. 7). Future work will be directed towards investigating whether the alternative definition of the Lie bracket in terms of the Jacobians can be used to obtain an estimate of the SPI, omitting the computationally expensive reconstruction of many paths per voxel required for the current method.

5.5 Future perspectives

Our results indicate that areas with high SPI values are relatively consistent between healthy subjects, and we therefore hypothesize that they could be used as new structural features of the brain. The extensiveness, orientation, and spatial distribution of sheet structures could be altered in the case of pathology. For example, if these sheets truly occur in the brain like “the warp and weft of fabric” (Wedeen et al., 2012a), it might be the case that space occupying lesions could dislocate the whole sheet structure as opposed to individual pathways. Another interesting feature could be the angle between pathways that form sheets through the shape of sheet tensors; it was shown that there was a significant crossing-angle difference in the frontal connections between a schizophrenia and healthy control group (Pasternak et al., 2012). The hypothesis that sheet structures have a close connection to development, axonal path finding, and the chemotactic gradients of early embryogenesis (Wedeen et al., 2012b) can now be investigated in a quantitative fashion. Whereas we only visually confirmed the consistency of areas with high SPI values between subjects in this work, a quantitative evaluation should be performed in future work. Such an inter-subject or inter-group evaluation would require a way to register these structures towards each other. Preliminary results of a quantitative comparison in which we registered the FA images of HCP subjects and calculated the overlap of thresholded maximum SPI maps indicated only a moderate overlap (Fig. S9). However, in analogy to recent insights in tract-based analyses, it is likely not optimal to work in voxel coordinate space and register scalar volumes such as FA, since such methods can for example not distinguish between nearby but differently oriented tracts

(O'Donnell et al., 2009). Instead, point correspondences should be found 'in the space of sheet structures'. Ongoing developments in registration of tensor fields (e.g. (Zhang et al., 2006a) which could potentially be applied to sheet tensors), ODFs and multi-fascicle models (e.g. (Raffelt et al., 2011; Taquet et al., 2014)), and tractography data (e.g. (Garyfallidis et al., 2015; O'Donnell et al., 2012)) could contribute towards this end.

Although we find that the dMRI data investigated in this work supports the existence of sheet-like structures at certain locations in the brain, it should be noted that the dMRI data reflects just a few aspects of the true underlying structure and its derived tracts do not correspond to true axons. Ideally, the existence of sheet structure should also be validated with a 'gold standard', such as histology, and quantified with other techniques that can map brain structure orientations. Exciting new technologies such as CLARITY (Chung et al., 2013) and polarized light imaging (Axer et al., 2001) could provide more insight into the existence of sheet structures and the scale on which they exist. Our method can be used in combination with such techniques: the Lie bracket computation is based on vector fields and could therefore be extended to directional data derived from these other techniques.

6. Conclusion

The extensive presence of sheet structures in the brain has been debated since its proposal, mainly due to its unclear relation to orthogonal angles and a lack of quantitative characterization. In this work we have explored the necessary and sufficient condition for a sheet structure to exist, which involves the computation of the Lie bracket of vector fields. We have proposed a method to compute the Lie bracket throughout the brain taking into account challenges such as discretization, noise, and clustering of vector fields. We have proposed a novel metric based on the Lie bracket, the sheet probability index (SPI), which indicates the extent to which the data supports sheet structure. In simple vector field and diffusion MRI simulations the method is able to quantitatively distinguish sheet from non-sheet structure, with spatial resolution and SNR being important factors that influence the accuracy and precision. Real diffusion MRI data experiments reveal a high SPI at various locations in the brain at the investigated scale, but also low SPI areas were found. Several high SPI areas could consistently be recognized across subjects, scanners, diffusion MRI techniques (i.e. CSD vs DSI), and spatial resolutions. Neither CSD nor DSI finds a high SPI at every location in the brain, and we find no bias towards sheet structure for DSI. Since tractography pathways do not represent true axons, validation of sheet structure with other technologies is necessary, and the proposed method can be extended to quantify sheet structure in other directional data. We hypothesize that sheet structure location, extent, and orientation could serve as new and important structural features of the brain.

Supplementary Material

Refer to Web version on PubMed Central for supplementary material.

Acknowledgments

The authors thank many colleagues in the field for useful discussions. Maxime Chamberland is acknowledged for help with visualization using the FiberNavigator. C.T. is supported by a grant (No. 612.001.104) from the Physical

Sciences division of the Netherlands Organization for Scientific Research (NWO), and is grateful to dr. ir. Marina van Damme and University Fund Eindhoven for financial support. The research of A.L. is supported by VIDI Grant 639.072.411 from NWO. T.D. gratefully acknowledges NWO (No 617.001.202) for financial support. The authors acknowledge the NIH grants R01MH074794, P41EB015902, P41EB015898. Data were provided in part by the Human Connectome Project, WU-Minn Consortium (Principal Investigators: David Van Essen and Kamil Ugurbil; 1U54MH091657) funded by the 16 NIH Institutes and Centers that support the NIH Blueprint for Neuroscience Research; and by the McDonnell Center for Systems Neuroscience at Washington University. Data collection and sharing for this project was provided in part by the MGH-USC Human Connectome Project (HCP; Principal Investigators: Bruce Rosen, M.D., Ph.D., Arthur W. Toga, Ph.D., Van J. Wedeen, MD). HCP funding was provided by the National Institute of Dental and Craniofacial Research (NIDCR), the National Institute of Mental Health (NIMH), and the National Institute of Neurological Disorders and Stroke (NINDS). HCP data are disseminated by the Laboratory of Neuro Imaging at the University of California, Los Angeles.

Reference List

- Assaf Y, Blumenfeld-Katzir T, Yovel Y, Basser PJ. AxCaliber: a method for measuring axon diameter distribution from diffusion MRI. *Magn Reson Med*. 2008; 59:1347–1354. [PubMed: 18506799]
- Astola L, Fuster A, Florack L. A Riemannian scalar measure for diffusion tensor images. *Pattern Recognition*. 2011; 44:1885–1891.
- Axer H, Axer M, Krings T, Keyserlingk DG. Quantitative estimation of 3-D fiber course in gross histological sections of the human brain using polarized light. *J Neurosci Methods*. 2001; 105:121–131. [PubMed: 11275269]
- Callaghan PT, MacGowan D, Packer KJ, Zelaya FO. High-resolution q-space imaging in porous structures. *Journal of Magnetic Resonance* (1969). 1990; 90:177–182.
- Catani M, Bodi I, Dell'acqua F. Comment on “The geometric structure of the brain fiber pathways”. *Science*. 2012; 337:1605.
- Chamberland M, Whittingstall K, Fortin D, Mathieu D, Descoteaux M. Real-time multipeak tractography for instantaneous connectivity display. *Front Neuroinform*. 2014; 8:59. [PubMed: 24910610]
- Chen YH, Wei D, Newstadt G, DeGraef M, Simmons J, Hero A. Parameter estimation in spherical symmetry groups. *Signal Processing Letters, IEEE*. 2015; 22:1152–1155.
- Chung K, Wallace J, Kim SY, Kalyanasundaram S, Andalman AS, Davidson TJ, Mirzabekov JJ, Zalocusky KA, Mattis J, Denisin AK, Pak S, Bernstein H, Ramakrishnan C, Grose L, Gradinaru V, Deisseroth K. Structural and molecular interrogation of intact biological systems. *Nature*. 2013; 497:332–337. [PubMed: 23575631]
- Daducci A, Dal PA, Lemkaddem A, Thiran JP. COMMIT: Convex optimization modeling for microstructure informed tractography. *IEEE Trans Med Imaging*. 2015; 34:246–257. [PubMed: 25167548]
- Dell'Acqua F, Rizzo G, Scifo P, Clarke RA, Scotti G, Fazio F. A model-based deconvolution approach to solve fiber crossing in diffusion-weighted MR imaging. *IEEE Trans Biomed Eng*. 2007; 54:462–472. [PubMed: 17355058]
- Dell'Acqua F, Scifo P, Rizzo G, Catani M, Simmons A, Scotti G, Fazio F. A modified damped Richardson-Lucy algorithm to reduce isotropic background effects in spherical deconvolution. *Neuroimage*. 2010; 49:1446–1458. [PubMed: 19781650]
- Dell'acqua F, Simmons A, Williams SC, Catani M. Can spherical deconvolution provide more information than fiber orientations? Hindrance modulated orientational anisotropy, a true-tract specific index to characterize white matter diffusion. *Hum Brain Mapp*. 2013; 34:2464–2483. [PubMed: 22488973]
- Ferizi U, Schneider T, Panagiotaki E, Nedjati-Gilani G, Zhang H, Wheeler-Kingshott CA, Alexander DC. A ranking of diffusion MRI compartment models with in vivo human brain data. *Magn Reson Med*. 2014; 72:1785–1792. [PubMed: 24347370]
- Fieremans E, Jensen JH, Helpert JA. White matter characterization with diffusional kurtosis imaging. *NeuroImage*. 2011; 58:177–188. [PubMed: 21699989]
- Froeling M, Tax CMW, Vos SB, Luijten PR, Leemans A. The “MASSIVE” brain dataset: Multiple Acquisitions for Standardization of Structural Imaging Validation and Evaluation. *Magnetic resonance in medicine*. 2016

- Garyfallidis E, Ocegueda O, Wassermann D, Descoteaux M. Robust and efficient linear registration of white-matter fascicles in the space of streamlines. *NeuroImage*. 2015; 117:124–140. [PubMed: 25987367]
- Glasser MF, Sotiropoulos SN, Wilson JA, Coalson TS, Fischl B, Andersson JL, Xu J, Jbabdi S, Webster M, Polimeni JR, Van Essen DC, Jenkinson M. The minimal preprocessing pipelines for the Human Connectome Project. *Neuroimage*. 2013; 80:105–124. [PubMed: 23668970]
- Jeurissen B, Leemans A, Jones DK, Tournier JD, Sijbers J. Probabilistic fiber tracking using the residual bootstrap with constrained spherical deconvolution. *Hum Brain Mapp*. 2011; 32:461–479. [PubMed: 21319270]
- Jeurissen B, Leemans A, Tournier JD, Jones DK, Sijbers J. Investigating the prevalence of complex fiber configurations in white matter tissue with diffusion magnetic resonance imaging. *Hum Brain Mapp*. 2013; 34:2747–2766. [PubMed: 22611035]
- Jones DK. Challenges and limitations of quantifying brain connectivity in vivo with diffusion MRI. *Imaging*. 2010; 2:341–355.
- Kindlmann G, Tricoche X, Westin CF. Delineating white matter structure in diffusion tensor MRI with anisotropy creases. *Medical Image Analysis*. 2007; 11:492–502. [PubMed: 17804278]
- Lang, S. *Differential and Riemannian Manifolds*, Graduate Texts in Mathematics ed. Springer-Verlag; New York: 1995.
- Leemans, A., Jeurissen, B., Sijbers, J., Jones, DK. ExploreDTI: a graphical toolbox for processing, analyzing, and visualizing diffusion MR data. *Proceedings of the 17nd Annual Meeting of the ISMRM*; 2009. p. 3537
- Leemans A, Sijbers J, De BS, Vandervliet E, Parizel P. Multiscale white matter fiber tract coregistration: a new feature-based approach to align diffusion tensor data. *Magn Reson Med*. 2006; 55:1414–1423. [PubMed: 16685732]
- Mardia, KV., Jupp, PE. *Directional statistics*. 494. Wiley.com; 2009.
- Misner, CW., Thorne, KS., Wheeler, JA. *Gravitation*. W. H. Freeman; 1973.
- Mori S, van Zijl PC. Fiber tracking: principles and strategies - a technical review. *NMR Biomed*. 2002; 15:468–480. [PubMed: 12489096]
- O'Donnell LJ, Wells WM III, Golby AJ, Westin CF. Unbiased groupwise registration of white matter tractography. *Med Image Comput Comput Assist Interv*. 2012; 15:123–130. [PubMed: 23286122]
- Pasternak, O., Rathi, Y., Shenton, M., Westin, CF. Estimation of the Angle Between Crossing Fibers as a Novel Structural Quantity. *Proceedings of the 20th Annual Meeting of the ISMRM*; 2012. p. 1915
- Raffelt D, Tournier JD, Fripp J, Crozier S, Connelly A, Salvado O. Symmetric diffeomorphic registration of fibre orientation distributions. *Neuroimage*. 2011; 56:1171–1180. [PubMed: 21316463]
- Raffelt D, Tournier JD, Rose S, Ridgway GR, Henderson R, Crozier S, Salvado O, Connelly A. Apparent Fibre Density: a novel measure for the analysis of diffusion-weighted magnetic resonance images. *Neuroimage*. 2012; 59:3976–3994. [PubMed: 22036682]
- Reisert M, Kiselev VG, Dihtal B, Kellner E, Novikov DS. MesoFT: unifying diffusion modelling and fiber tracking. *Med Image Comput Comput Assist Interv*. 2014; 17:201–208. [PubMed: 25320800]
- Savadjiev P, Rathi Y, Bouix S, Verma R, Westin CF. Multi-scale characterization of white matter tract geometry. *Med Image Comput Comput Assist Interv*. 2012; 15:34–41.
- Schultz T, Theisel H, Seidel HP. Crease surfaces: from theory to extraction and application to diffusion tensor MRI. *IEEE Trans Vis Comput Graph*. 2010; 16:109–119. [PubMed: 19910665]
- Setsompop K, Kimmlingen R, Eberlein E, Witzel T, Cohen-Adad J, McNab JA, Keil B, Tisdall MD, Hoecht P, Dietz P, Cauley SF, Tountcheva V, Matschl V, Lenz VH, Heberlein K, Potthast A, Thein H, Van HJ, Toga A, Schmitt F, Lehne D, Rosen BR, Wedeen V, Wald LL. Pushing the limits of in vivo diffusion MRI for the Human Connectome Project. *NeuroImage*. 2013; 80:220–233. [PubMed: 23707579]
- Smith SM, Jenkinson M, Johansen-Berg H, Rueckert D, Nichols TE, Mackay CE, Watkins KE, Ciccarelli O, Cader MZ, Matthews PM, Behrens TE. Tract-based spatial statistics: voxelwise analysis of multi-subject diffusion data. *Neuroimage*. 2006; 31:1487–1505. [PubMed: 16624579]

- Sotiropoulos SN, Jbabdi S, Xu J, Andersson JL, Moeller S, Auerbach EJ, Glasser MF, Hernandez M, Sapiro G, Jenkinson M, Feinberg DA, Yacoub E, Lenglet C, Van Essen DC, Ugurbil K, Behrens TE. Advances in diffusion MRI acquisition and processing in the Human Connectome Project. *Neuroimage*. 2013; 80:125–143. [PubMed: 23702418]
- Spivak, M. A comprehensive introduction to differential geometry. Publish or Perish, inc; 1979.
- Taquet M, Scherrer B, Commowick O, Peters JM, Sahin M, Macq B, Warfield SK. A mathematical framework for the registration and analysis of multi-fascicle models for population studies of the brain microstructure. *IEEE Trans Med Imaging*. 2014; 33:504–517. [PubMed: 24235301]
- Tax, CMW., Dela Haije, T., Fuster, A., Duits, R., Viergever, MA., Calabrese, E., Johnson, GA., Florack, LMJ., Leemans, A. International BASP Frontiers Workshop. 2015. Towards quantification of the brain's sheet structure in diffusion MRI data; p. 74
- Tax, CMW., Dela Haije, T., Fuster, A., Duits, R., Viergever, MA., Florack, LMJ., Leemans, A. Towards quantification of the brain's sheet structure: Evaluation of the discrete Lie bracket. *Proceedings of the 22nd Annual Meeting of the ISMRM*; 2014a. p. 0975
- Tax, CMW., Duits, R., Romeny, BM., Vilanova, A., Ossenkop, P. Tractography of the Optic Radiation for Vision Sparing Epilepsy Surgery. *Proceedings of the IEEE ICIA*; 2012. p. 441-445.
- Tax CMW, Jeurissen B, Vos SB, Viergever MA, Leemans A. Recursive calibration of the fiber response function for spherical deconvolution of diffusion MRI data. *NeuroImage*. 2014b; 86:67–80. [PubMed: 23927905]
- Tournier JD, Calamante F, Connelly A. Robust determination of the fibre orientation distribution in diffusion MRI: non-negativity constrained super-resolved spherical deconvolution. *Neuroimage*. 2007; 35:1459–1472. [PubMed: 17379540]
- Van Essen DC, Smith SM, Barch DM, Behrens TE, Yacoub E, Ugurbil K. The WU-Minn Human Connectome Project: an overview. *NeuroImage*. 2013; 80:62–79. [PubMed: 23684880]
- Vilanova, A., Berenschot, G., Van Pul, C. DTI visualization with streamsurfaces and evenly-spaced volume seeding. *Eurographics Association*; 2004. p. 173-182.
- Wang, R., Benner, T., Sorensen, AG., Wedeen, VJ. Diffusion Toolkit: A Software Package for Diffusion Imaging Data Processing and Tractography. *Proceedings of the 15th Annual Meeting of the ISMRM*; 2007. p. 3720
- Wedeen VJ, Hagmann P, Tseng WY, Reese TG, Weisskoff RM. Mapping complex tissue architecture with diffusion spectrum magnetic resonance imaging. *Magn Reson Med*. 2005; 54:1377–1386. [PubMed: 16247738]
- Wedeen, VJ., Mortazavi, F., Wang, R., Isaac Tseng, W., Witzel, T., Nummenmaa, A., Orrison, W., Tanley, HE., Ald, L., Osene, D. Grid structure of brain pathways - Validation and the character of turns. *Proceedings of the 22nd Annual Meeting of the ISMRM*; 2014. p. 0803
- Wedeen VJ, Rosene DL, Wang R, Dai G, Mortazavi F, Hagmann P, Kaas JH, Tseng WY. Response to comment on “the geometric structure of the brain fiber pathways”. *Science*. 2012a; 337:1605.
- Wedeen VJ, Rosene DL, Wang R, Dai G, Mortazavi F, Hagmann P, Kaas JH, Tseng WY. The geometric structure of the brain fiber pathways. *Science*. 2012b; 335:1628–1634. [PubMed: 22461612]
- Westin CF, Maier SE, Mamata H, Nabavi A, Jolesz FA, Kikinis R. Processing and visualization for diffusion tensor MRI. *Med Image Anal*. 2002; 6:93–108. [PubMed: 12044998]
- Yushkevich PA, Zhang H, Simon TJ, Gee JC. Structure-specific statistical mapping of white matter tracts. *Neuroimage*. 2008; 41:448–461. [PubMed: 18407524]
- Zhang H, Schneider T, Wheeler-Kingshott CA, Alexander DC. NODDI: practical in vivo neurite orientation dispersion and density imaging of the human brain. *Neuroimage*. 2012; 61:1000–1016. [PubMed: 22484410]
- Zhang H, Yushkevich PA, Alexander DC, Gee JC. Deformable registration of diffusion tensor MR images with explicit orientation optimization. *Med Image Anal*. 2006a; 10:764–785. [PubMed: 16899392]
- Zhang J, van Zijl PC, Mori S. Image contrast using the secondary and tertiary eigenvectors in diffusion tensor imaging. *Magn Reson Med*. 2006b; 55:439–449. [PubMed: 16402380]
- Zhang M, Fletcher PT. Finite-Dimensional Lie Algebras for Fast Diffeomorphic Image Registration. *Inf Process Med Imaging*. 2015; 24:249–259. [PubMed: 26221678]

Zhang S, Demiralp C, Laidlaw DH. Visualizing diffusion tensor MR images using streamtubes and streamsurfaces. Visualization and Computer Graphics, IEEE Transactions on. 2003; 9:454–462.

Appendix

Appendix A: List of symbols

U, V, W, X, Y, Z, \dots	Vector fields, where a field X is defined on $N_X \subset \mathbb{R}^3$	S_{ij}	The cosine similarity between the i -th and j -th vector in an ordered set
$p, q \in M \subset \mathbb{R}^3$	Positions in the brain M	h	Discrete flow distance along an integral curve
X_p	Vector X at point p	h	Step size in a discrete flow
$S \subset \mathbb{R}^3$	Sheet structure	h_{max}	The maximum distance in a discrete flow
$\Phi^X(s, p), \hat{\Phi}_s^X(p)$	The flow operator, along X for a distance s and with initial position p	R, H, β, e	Matrices
R_p	The vector given by the deviation from p after specific flows, called the closure	P_λ	The sheet probability index with parameter λ
$[V, W]_p$	Lie bracket of V and W at point p	$\mathcal{N}(\mu, \sigma^2)$	Normal distribution with mean μ and standard deviation σ
$[V, W]_p^\perp$	Normal component of $[V, W]_p$	x^i	Cartesian coordinates
$\hat{\Phi}_s^X$	Discrete approximation to the flow Φ_s^X	T_p	Sheet tensor at p
$[\widehat{V, W}]_p$	Discrete Lie bracket of V and W at point p	$X_p \otimes X_p, X_p X_p^T$	Tensor product between two identical vectors X_p
\hat{R}	Estimated closure	κ, ρ	The curvature κ , and its reciprocal ρ
$[a, b, \dots]$	Ordered set of elements	δ	Voxel size
p	A permutation of an ordered set	N_r, N_b	The number of noise or bootstrap iterations
E	Similarity energy	b	The b -value

Appendix B: Mathematical background

There are three concepts that are explained or mentioned in the main text, which we feel might benefit from a more detailed exposition. These are the formal definition of the Lie bracket and its relation to the definition in terms of flows along vector fields (Section 3.1.2), the relation between the Lie bracket and the sheet structure (Sections 3.1.1 and 3.1.3), and the definition of three-dimensional grid structure (e.g. Section 1). In this appendix we discuss these more in-depth.

B.1 The Lie bracket and its relation to flow

In a *differentiable manifold* M , a *tangent vector* V_p at $p \in M$ is identified with the directional derivative (denoted by ∇_V) of any suitably differentiable function $f: M \rightarrow \mathbb{R}$. Hence we can

write $V_p f = \nabla_V f(p) = \sum_{i=1}^3 V^i \frac{\partial f}{\partial x^i}(p)$, given the components $\{V_1, V_2, V_3\}$ of V relative to the coordinates x_1, x_2, x_3 on M . Let $T_p M$ denote the space of all tangent vectors at $p \in M$, and let the *tangent bundle* TM represent the union $\{T_p M \mid p \in M\}$, i.e., the set of all tangent vectors in M . A vector field V is now defined as the smooth mapping $V: M \rightarrow TM: p \mapsto V_p$. The Lie bracket of two (non-zero) vector fields V and W on M is defined by its action on smooth functions f :

$$[V, W]_p(f) = V_p W(f) - W_p V(f) = \nabla_V \nabla_W f(p) - \nabla_W \nabla_V f(p). \quad [12]$$

The Lie bracket satisfies the defining properties of a derivative (linearity and Leibniz' product rule), and so $[V, W]_p$ can be regarded as a directional derivative, i.e. an element of the vector space $T_p M$. If one is interested specifically in the Lie bracket $[V, W]$ in terms of the vector fields V and W , Eq. [12] can be used to obtain

$$[V, W] = \nabla_V W - \nabla_W V, \quad [13]$$

which is commonly known as the commutator of the vector fields, and where $\nabla_V W$ denotes the derivative of W along V .

To relate the Lie bracket to flows $\Phi_t^V: M \rightarrow M: p \mapsto \Phi_t^V(p)$ we write, using Taylor's theorem,

$$\Phi_t^V(p) = \sum_{k=0}^{\infty} \frac{t^k}{k!} \left(\frac{d^k}{dt^k} \Big|_{t=0} \Phi_t^V(p) \right) = p + tV_p + \frac{1}{2}t^2 \nabla_V V + O(t^3). \quad [14]$$

Note that because $\frac{d}{dt} \Big|_{t=0} f(\Phi_t^V(p)) = V_p(f)$ for any suitably differentiable f (compare this to the definition $\frac{d}{dt} \Big|_{t=0} \Phi_t^V(p) = V_p$ used in the main text) it follows that $\frac{d}{dt} \Big|_{t=0} W_{\Phi_t^V(p)} = V_p W$. Taking $s(t) = t$ this gives

$$\begin{aligned} & \left(\Phi_{s(t)}^W \circ \Phi_t^V \right) (p) = \Phi_t^V(p) + s(t)W_{\Phi_t^V(p)} + \frac{1}{2}s(t)^2 W_{\Phi_t^V(p)}^2 W + O(s(t)^3) \\ & = p + tV_p + \frac{1}{2}t^2 \nabla_V V + O(t^3) + s(t)W_p + s(t)tV_p W + O(s(t)t^2) + \frac{1}{2}s(t)^2 W_p^2 W + O(s(t)^2 t) + O(s(t)^3), \end{aligned} \quad [15]$$

where we repeatedly apply Eq. [14], such that

$$(\Phi_t^W \circ \Phi_t^V)(p) = p + t(V_p + W_p) + t^2 V_p W + \frac{1}{2} t^2 (V_p V + W_p W) + O(t^3). \quad [16]$$

Continuing this process to compute $(\Phi_{s(t)}^{-V} \circ \Phi_t^W \circ \Phi_t^V)(p)$ and $(\Phi_{s(t)}^{-W} \circ \Phi_t^{-V} \circ \Phi_t^W \circ \Phi_t^V)(p)$, we then find

$$(\Phi_t^{-W} \circ \Phi_t^{-V} \circ \Phi_t^W \circ \Phi_t^V)(p) = p + t^2 (V_p W - W_p V) + O(t^3) = p + t^2 [V, W] + O(t^3), \quad [17]$$

after which Eq. [4] follows readily. Validity of the alternative definitions in Eq. [6] can be derived analogously. If V and W are defined on subsets N_V and N_W of M as in the main text, then the Lie bracket is only defined on the intersection $N_V \cap N_W$. In the remaining sections of this appendix we will continue with V and W defined on the whole of M .

B.2 Sheet structure and the Lie bracket

The flow $\Phi_t^V(p)$ defines a curve $t \mapsto \Phi_t^V(p)$. The curves obtained when varying p form the *leaves* of a one-dimensional *foliation* of M ; they are disjoint immersed submanifolds that partition M , which are tangent to V for all p and t . The existence of such a one-dimensional foliation given V is ensured by smoothness of V , but for higher-order foliations that are tangent to multiple vector fields there are additional constraints. These are summarily provided by the Lie bracket, which guarantees the existence of a foliation if the set of all vector fields that are locally tangent to the sheet, is closed under the Lie bracket.

For the existence of a two-dimensional foliation given two locally non-collinear vector fields V and W , it is sufficient if for all $p \in M$ we have $[V, W]_p \in \text{span}(V_p, W_p) \subset T_p M$, which is equivalent to the requirement $[V, W]^\perp = 0$ used in the main text. The fact that $[V, W]^\perp = 0$ is a necessary and sufficient condition for the existence of a foliation (with leaves that are locally perpendicular to both V and W) is known as the Frobenius theorem (Lang, 1995; Spivak, 1979). If V and W form a foliation, then all points on a leaf can be connected with a flow along these vector fields. The two-dimensional foliation of (a subset) of \mathbb{R}^3 is called the *sheet structure*.

B.3 Grid structure

Grid structure as introduced by Wedeen et al. (2012b) is finally defined as three independent two-dimensional foliations, which form a three-dimensional foliation. Given three independent vector fields U , V , and W on M , a sufficient condition for the existence of this structure is that the Lie bracket normal component of each pair of vector fields is zero. As was the case with sheet structure, grid structure ensures that any two points on the leaves of this foliation can be connected with a flow along the vector fields. In the considered case of \mathbb{R}^3 , this means that any two points in the entire space can be connected by means of such a flow: the flows along U , V , and W are coordinates lines.

Appendix C: Algorithms

C.1 Clustering of frames

Consider an *ordered set* of n vectors $[Y_1, \dots, Y_n]$ at a position q , and m vectors $\{Z_1, \dots, Z_m\}$ in some point r near q^3 . The ordered set $[Y_1, \dots, Y_n]$ serves as a *reference frame*, i.e., we assume that n vector fields U, V, \dots are present in the local neighborhood of q that satisfy $U_q = Y_1, V_q = Y_2, \dots$. The aim of the clustering algorithm is to find a permutation of the frame (an ordered set $[Z_{p_1}, \dots, Z_{p_n}, 0, \dots]$) that corresponds to the reference frame, so that we can take $U_r = Z_{p_1}, V_r = Z_{p_2}, \dots$ for some *permutation* P of $[1, \dots, n]$ (see Fig. 3 for a schematic example). Here, P_i denotes the index given by the i^{th} element of P , and $Z_{P_i} = 0$ implies that no matching vector was found.

Clustering is done by maximizing (over all permutations P) a *similarity measure* E that represents the total element-wise similarity between the frames $[Y_1, \dots, Y_n]$ and $[Z_{p_1}, \dots, Z_{p_n}]$. In the algorithm below we will use the ‘total cosine similarity’ for E , which is defined as the sum of the cosines of the angles between corresponding vectors. The steps of our algorithm are as follows:

Algorithm for the clustering of frame $\{Z_1, \dots, Z_m\}$ given an ordered frame $[Y_1, \dots, Y_n]$

1. Compute the cosine similarity S_{ij} between Y_i and Z_j for all $i \in \{1, \dots, n\}, j \in \{1, \dots, m\}$ (recall that Y_i and Z_j are unit or zero vectors):

$$S_{ij} = |Y_i \cdot Z_j|. \quad [18]$$

2. For every n -permutation P of $[1, \dots, m]$ (e.g. for $n = 2$ and $m = 3$ these are the permutations $[1,2], [2,1], [1,3], [3,1], [2,3]$, and $[3,2]$), compute the similarity energy of the permutation by:

$$E_P = \sum_{i=1}^n S_{iP_i} \quad [19]$$

(e.g. for $P = [2,3]$ in the example above, which associates Z_2 to Y_1 and Z_3 to Y_2 , we have $E_P = S_{12} + S_{23}$). Note that taking the sum (as opposed to the mean) favors the assignment of more vectors.

3. Determine the permutation P for which E_P is maximal, and define the reordered set of vectors $[Z_{p_1}, \dots, Z_{p_n}]$.
4. If $Y_i \cdot Z_{P_i}$ has a negative sign, set Z_{P_i} to $-Z_{P_i}$.
5. Apply an angle threshold on Z_{P_i} . If $|Y_i \cdot Z_{P_i}| < t$ (here set to $\cos 35^\circ$) for some threshold $t \in \mathbb{R}$, set Z_{P_i} to 0.

³If $m < n$, we append $n - m$ zero-vectors to the list $\{Z_1, \dots, Z_m\}$, so in the following we can take $m = n$.

6. Return $[Z_{p_1}, \dots, Z_{p_n}]$.

C.2 Frame tractography

Algorithm for the approximate flow $\hat{\Phi}_h^X$ along vector field X from point q_0

1. While the number of taken steps J is less than or equal to a preset number of steps $L = \lfloor L/h \rfloor$ (where $\lfloor \cdot \rfloor$ denotes the floor function), do the following:
 - a. Move from the current position q_J in the direction X_{q_J} with step size h . The new position q_{J+1} is given by

$$q_{J+1} = q_J + \Delta h \cdot X_{q_J}. \quad [20]$$

- b. Identify the frame $\{Z_1, \dots, Z_m\}$ at location q_{J+1} .
 - c. Determine $[U_{q_{J+1}}, V_{q_{J+1}}, \dots]$ from $\{Z_1, \dots, Z_m\}$ with the algorithm described in Section 3.1.1, using $[U_{q_J}, V_{q_J}, \dots]$ as a reference frame. If $X_{q_J} = 0$, i.e., if X is not defined at the new location, the propagation is terminated.
2. Return $q_L = \hat{\Phi}_h^X(q_0)$ and the corresponding frame $[U_{q_L}, V_{q_L}, \dots]$.

C.3 The closure and the Lie bracket

Algorithm for the reconstruction of difference vector \hat{R}_1 at point p

1. Identify the frame $[Y_1, \dots, Y_n]$ at p , and set $U_p = Y_1, V_p = Y_2, \dots$. In practice, determining $\{Y_1, \dots, Y_n\}$ involves some kind of interpolation (e.g., nearest neighbor, trilinear) and potentially the computation of peak directions from dMRI data if one does not start from a set of pre-extracted peaks (see Section 3.4.2.3 for details). Here, we stick to a general formulation and assume that the frame $[Y_1, \dots, Y_n]$ is given or can be calculated.
2. Select two vectors Y_i and Y_j from $\{U, V, \dots\}$ for the computation of the Lie bracket, which could be, for example, peaks along two predefined tracts. Here, we take the example $Y_i \in V$ and $Y_j \in W$.
3. Starting from $q_0 = p$, compute the end point of the first leg $\hat{\Phi}_{h_1}^V(p)$ and the corresponding frame using the algorithm described in Section 3.1.2. If the tracking algorithm fails, the reconstruction algorithm is terminated.
4. Repeat step 3 with $q_0 = \hat{\Phi}_{h_1}^V(p)$ to compute the end point of the second leg $\hat{\Phi}_{h_2}^W \circ \hat{\Phi}_{h_1}^V(p)$.
5. Repeat step 3 with $q_0 = (\hat{\Phi}_{h_2}^W \circ \hat{\Phi}_{h_1}^V)(p)$ to compute the end point of the third leg $(\hat{\Phi}_{h_1}^{-V} \circ \hat{\Phi}_{h_2}^W \circ \hat{\Phi}_{h_1}^V)(p)$.

6. Repeat step 3 with $q_0 = \left(\hat{\Phi}_{h_1}^{-V} \circ \hat{\Phi}_{h_2}^W \circ \hat{\Phi}_{h_1}^V \right) (p)$ to compute the end point of the final leg $\left(\hat{\Phi}_{h_2}^{-W} \circ \hat{\Phi}_{h_1}^{-V} \circ \hat{\Phi}_{h_2}^W \circ \hat{\Phi}_{h_1}^V \right) (p)$.
7. Return $\hat{R}_1 = \left(\hat{\Phi}_{-h_2}^W \circ \hat{\Phi}_{-h_1}^V \circ \hat{\Phi}_{h_2}^W \circ \hat{\Phi}_{h_1}^V \right) (p) - p$.

When computing \hat{R} for all h_1 and h_2 , (parts of) paths are taken multiple times. The positions q and the corresponding frames for each path are therefore stored in a lookup table.

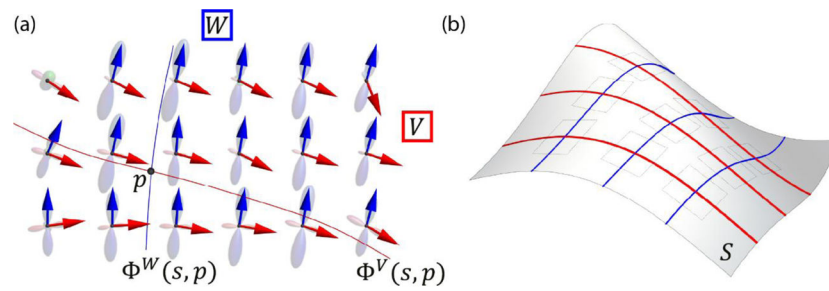


Fig. 1.

(a) An example set of fiber ODFs (semi-transparent) along with their peak directions (arrows), which form the vector fields V (red) and W (blue). By integrating these vector fields, one can reconstruct at each initial position p the integral curves $\Phi^V(s, p)$ (red curve) and $\Phi^W(s, p)$ (blue curve) where s denotes arc length parameterization. (b) The tangent plane of an integral surface S at any point $p \in S$ is parallel to the plane spanned by V_p and W_p (indicated by the dashed squares annotated on S).

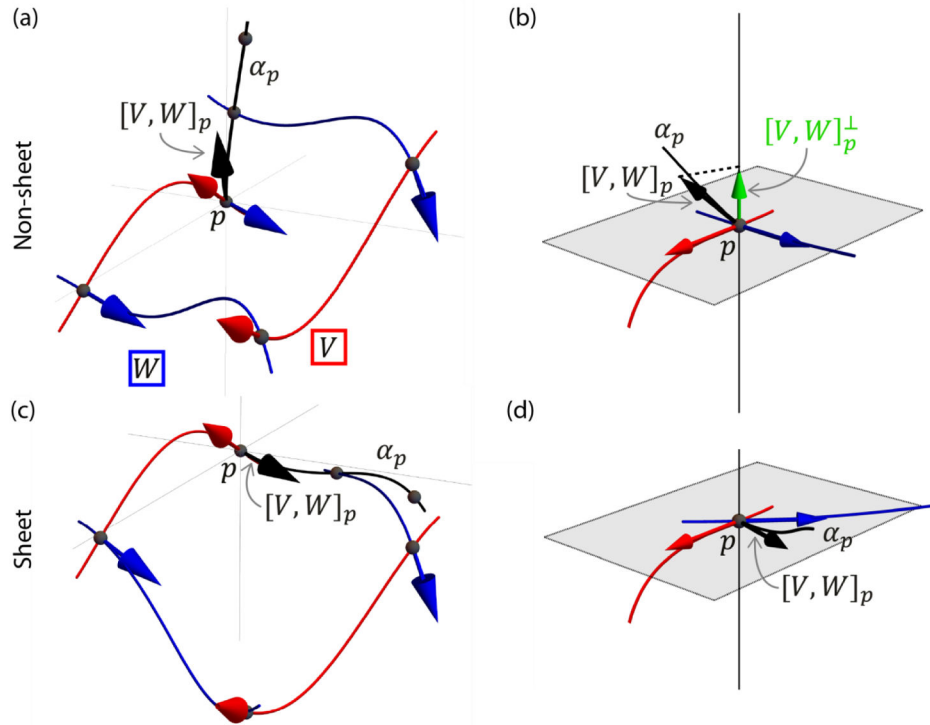


Fig. 2.

(a) A loop composed of integral curves of V (red arrows) and W (blue arrows) with p as the starting position. α_p is the curve formed by the end points of all loops (by varying the distance s) starting in the point p . $[V, W]_p$ is the Lie bracket at point p , and has a relation with the difference vector $R_p(s) = \alpha_p(s) - p$ according to Eq. [4]. In this scenario, the vector fields V and W cannot be integrated to form a sheet structure. (b) The Lie bracket from (a) does not lie in the plane spanned by V_p and W_p (gray). Hence the normal component of the Lie bracket $[V, W]_p^\perp$ defined in Eq. [5] is non-zero (green arrow), and the vector fields cannot be integrated to form a sheet structure. The vertical black line is perpendicular to the plane spanned by V_p and W_p . (c) A loop in a scenario where the vector fields V (red arrows) and W (blue arrows) do form a sheet structure. In this case α_p is (locally) a curve on the sheet structure. (d) The Lie bracket $[V, W]_p$ from (c) lies in the plane spanned by the vectors at p , so that the normal component is zero and the vector fields V and W can be integrated to form a two-dimensional sheet.

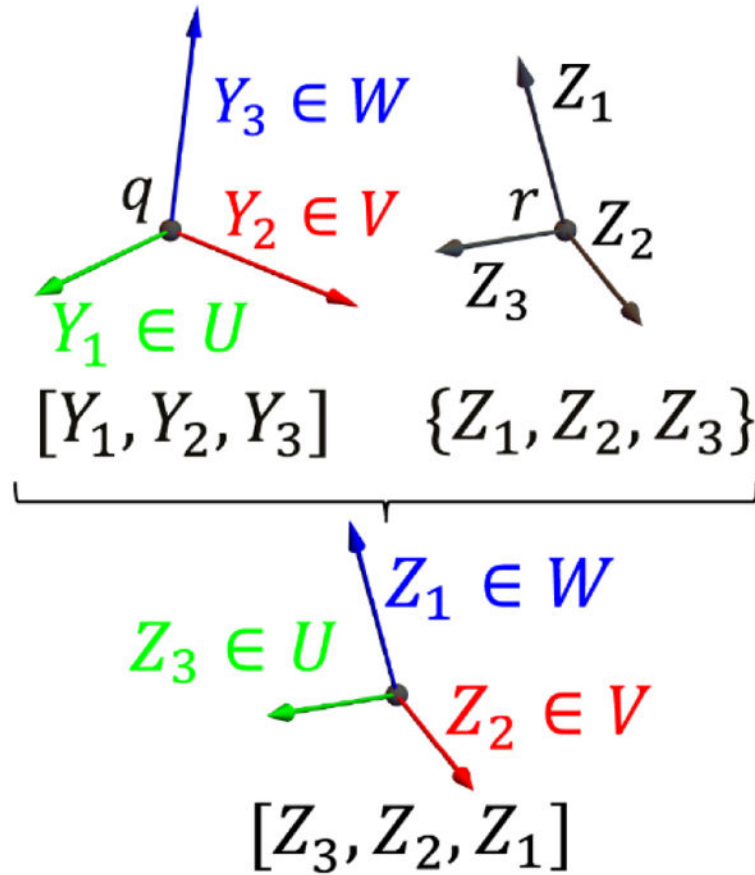


Fig. 3.

Example of the clustering of frames. We have an ordered set of vectors $[Y_1, Y_2, Y_3]$ at a position q , and 3 vectors $\{Z_1, Z_2, Z_3\}$ in some point r near q . We assume that they are assigned to the vector fields U , V , and W as follows: $U_q = Y_1$, $V_q = Y_2$, and $W_q = Y_3$. Frame clustering yields the ordered set $[Z_3, Z_2, Z_1]$.

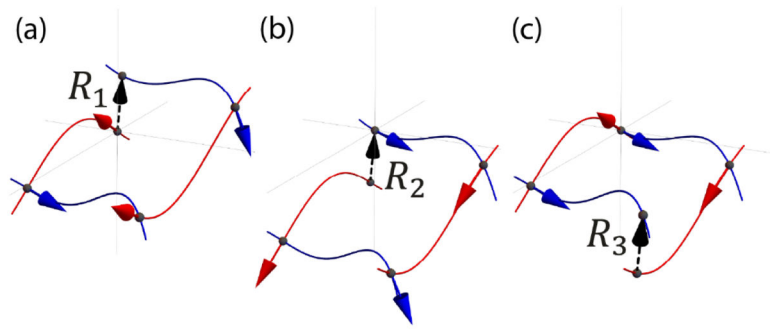


Fig. 4.

Loops that lead to

$$\hat{R}_1 := \left(\hat{\Phi}_{h_2}^{-W} \circ \hat{\Phi}_{h_1}^{-V} \circ \hat{\Phi}_{h_2}^W \circ \hat{\Phi}_{h_1}^V \right) (p) - p, \quad \hat{R}_2 := p - \left(\hat{\Phi}_{h_1}^{-V} \circ \hat{\Phi}_{h_2}^{-W} \circ \hat{\Phi}_{h_2}^W \right) (p) \text{ and}$$

$$\hat{R}_3 := \left(\hat{\Phi}_{h_2}^W \circ \hat{\Phi}_{h_1}^V \right) (p) - \left(\hat{\Phi}_{h_1}^V \circ \hat{\Phi}_{h_2}^W \right) (p).$$

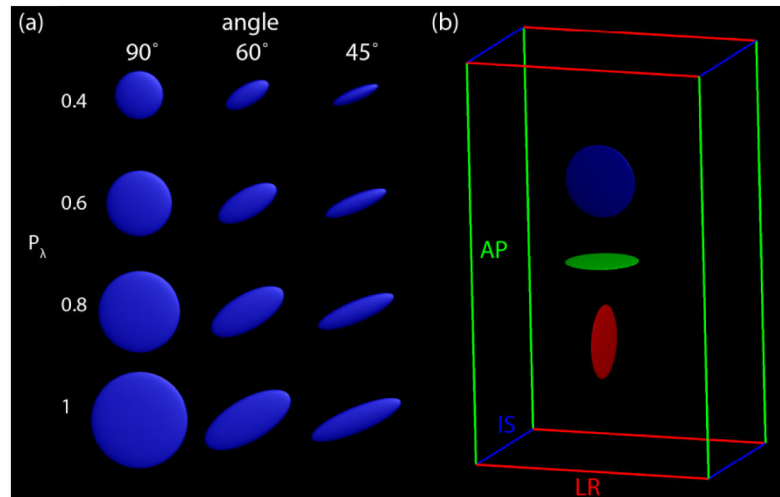


Fig. 5. (a) Sheet tensors with a normal direction pointing towards the reader, for different angles between U_p and V_p and different sheet probabilities. Here, V is always oriented in left-right direction. (b) Sheet tensors with different orientations are colored according to their third eigenvector. AP is the anterior-posterior direction, IS is inferior-superior, and LR is left-right.

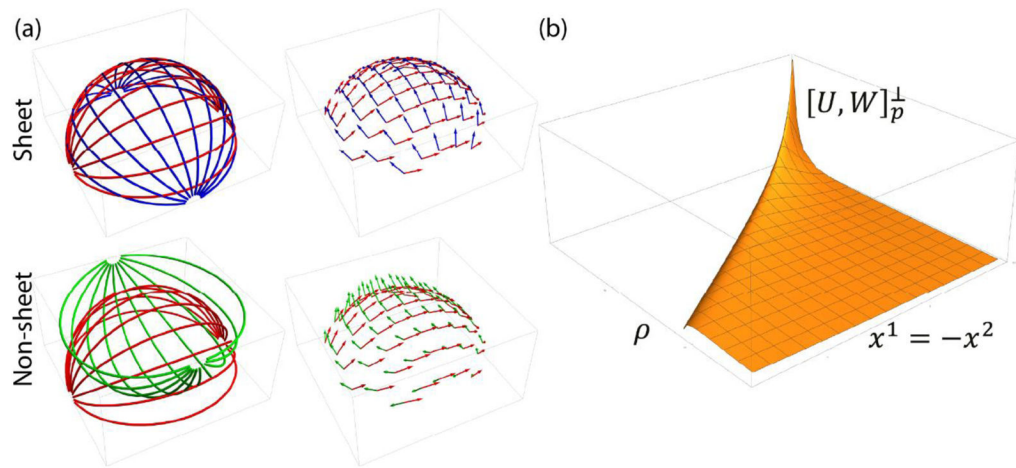


Fig. 6.

(a) Vector fields U (red), V (blue), and W (green), where U and V form a sheet and U and W do not. The left column shows a subset of integral curves, and vectors sampled on the upper hemisphere are shown on the right. This pattern of vector fields is repeated in the vertical direction. (b) Plot of $[U, W]_p^\perp$ as a function of ρ and x^1 , with $x^2 = -x^1$.

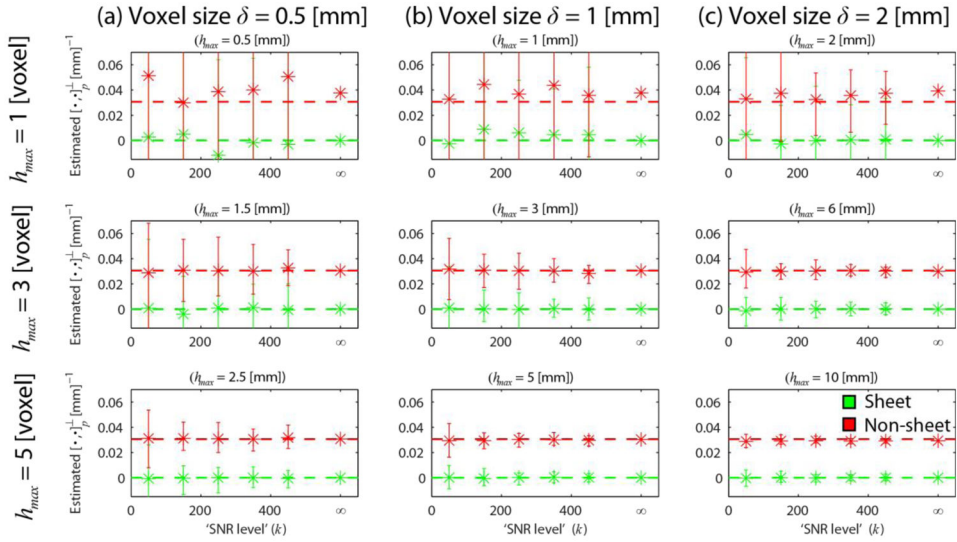
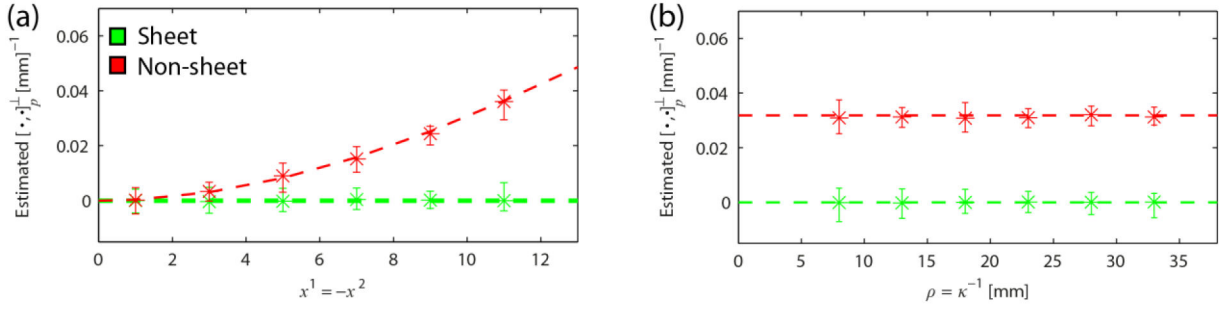


Fig. 7.

$[\hat{\cdot}]_p^\perp$ for different voxel sizes $\delta = \{0.5, 1, 2\}$ mm (a–c, columns) and different settings for $h_{max} = \{1, 3, 5\}$ voxels (the corresponding h_{max} in mm is noted above each plot). Each plot shows the mean and range of the estimates in the case of sheet (green, $[U, V]_p^\perp = 0$ indicated by the dashed line) and non-sheet (red, $[U, W]_p^\perp = 0.031$) for different SNR levels (i.e. the concentration parameter k , higher k means a lower perturbation of the vectors). We used 50 noise iterations, $\kappa = 1/\rho = 1/26$ mm⁻¹, and $p = (10, -10, 0)$.

**Fig. 8.**

(a) Mean and range of $[\widehat{\cdot}, \widehat{\cdot}]_p^\perp$ for different points $p = (x^1, -x^1, 0)$ to vary the Lie bracket normal component magnitude $[U, W]_p^\perp$ ($\kappa = 1/26 \text{ mm}^{-1}$). (b) Mean and range of $[\widehat{\cdot}, \widehat{\cdot}]_p^\perp$ for different curvatures $\kappa = 1/\{8, 13, 18, 23, 28, 33\}$. Different curvatures were achieved by changing ρ in Eq. [9], and $[U, W]_p^\perp$ was kept constant using Eq. [10] by adapting the point of evaluation $x^2 = -x^1$. In both experiments, $[U, V]_p^\perp$ (dashed lines) is evaluated at the same points for reference and $k = 350$, $\delta = 1 \text{ mm}$, and $h_{max} = 5 \text{ voxels}$.

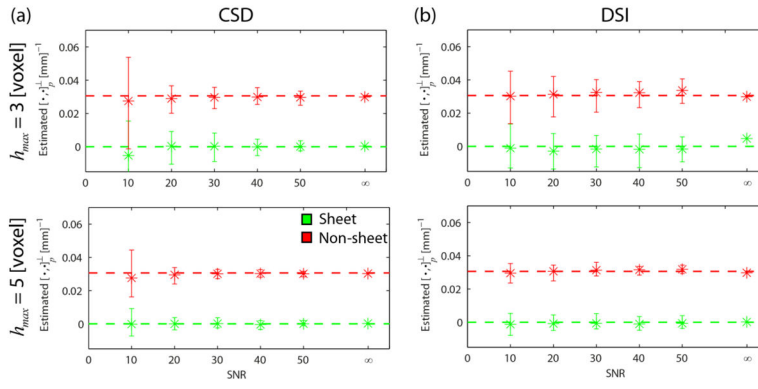


Fig. 9.

Mean and range of $[\widehat{\cdot}, \widehat{\cdot}]_p^\perp$ for different settings of h_{max} (rows) and different SNR. We set the curvature $\kappa = 1/\rho = 1/26 \text{ mm}^{-1}$, voxel size $\delta = 1 \text{ mm}$ (giving $h_{max} = \{3, 5\} \text{ voxels} = \{3, 5\} \text{ mm}$), and evaluate $[\widehat{\cdot}, \widehat{\cdot}]_p^\perp$ at $p = (10, -10, 0)$. Dashed lines indicate the true Lie bracket normal component. (a) Peaks extracted from single shell data using CSD. (b) Peaks extracted from Cartesian sampled data using DSI.

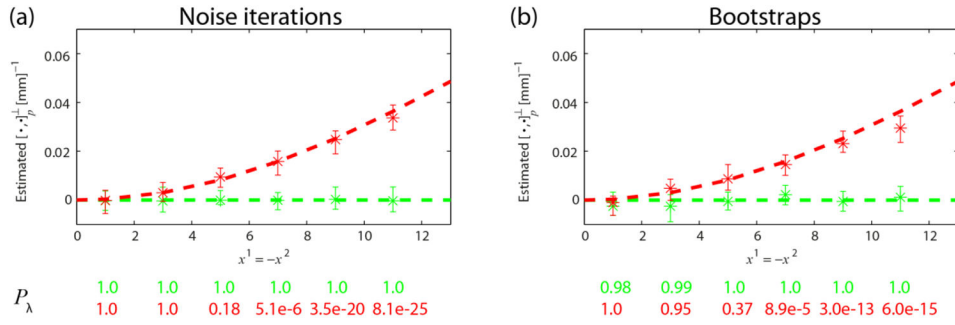


Fig. 10.

Mean and range of $[\widehat{\cdot}]_p^\perp$ and the SPI P_λ for different points $p = (x^1, -x^1, 0)$ to vary the Lie bracket normal component magnitude $[U, W]_p^\perp \cdot [U, V]_p^\perp$ is evaluated at the same points for reference. We set $\text{SNR} = 20$, $\delta = 1 \text{ mm}$, $h_{\text{max}} = 5 \text{ voxels}$, and $\kappa = 1/26 \text{ mm}^{-1}$.

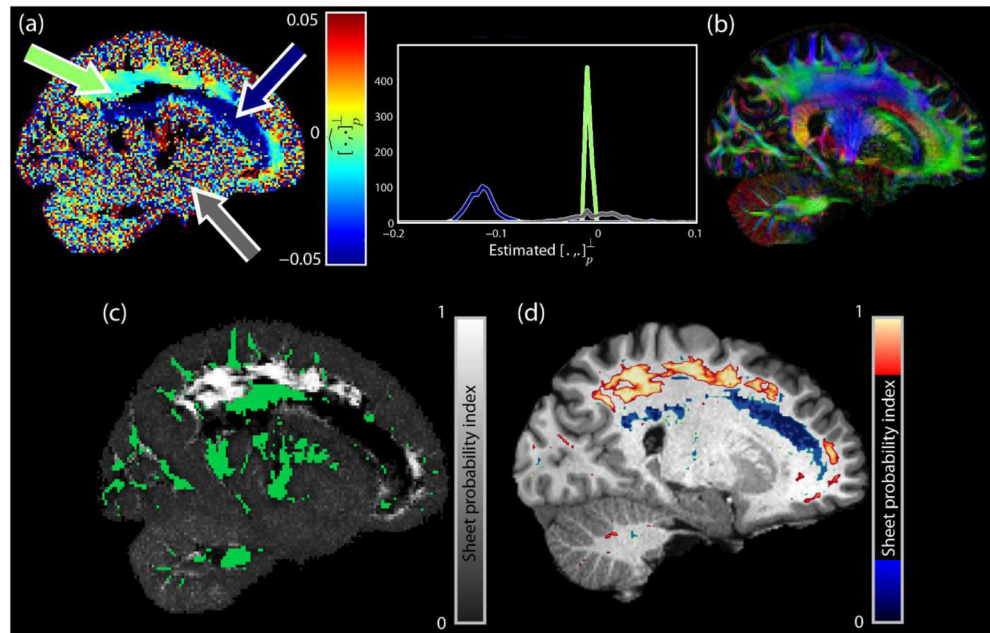


Fig. 11.

(a) A single bootstrap of the Lie bracket normal component (two largest fODF peaks) in a single slice, together with histograms of the normal component at the indicated locations in (high- (green arrow), medium- (grey arrow), and low-sheet probability (blue arrow) area). (b) A direction color-encoded FA map of the slice shown in (a) provided for reference. (c) The corresponding SPI map (maximum per voxel) with $\lambda = 0.008$. The green voxels only contain one peak and thus no Lie bracket can be computed. (d) The high- (red, $P_\lambda > 0.5$) and low-sheet probability areas (blue, $P_\lambda < 0.1$) shown as an overlay on an anatomical scan.

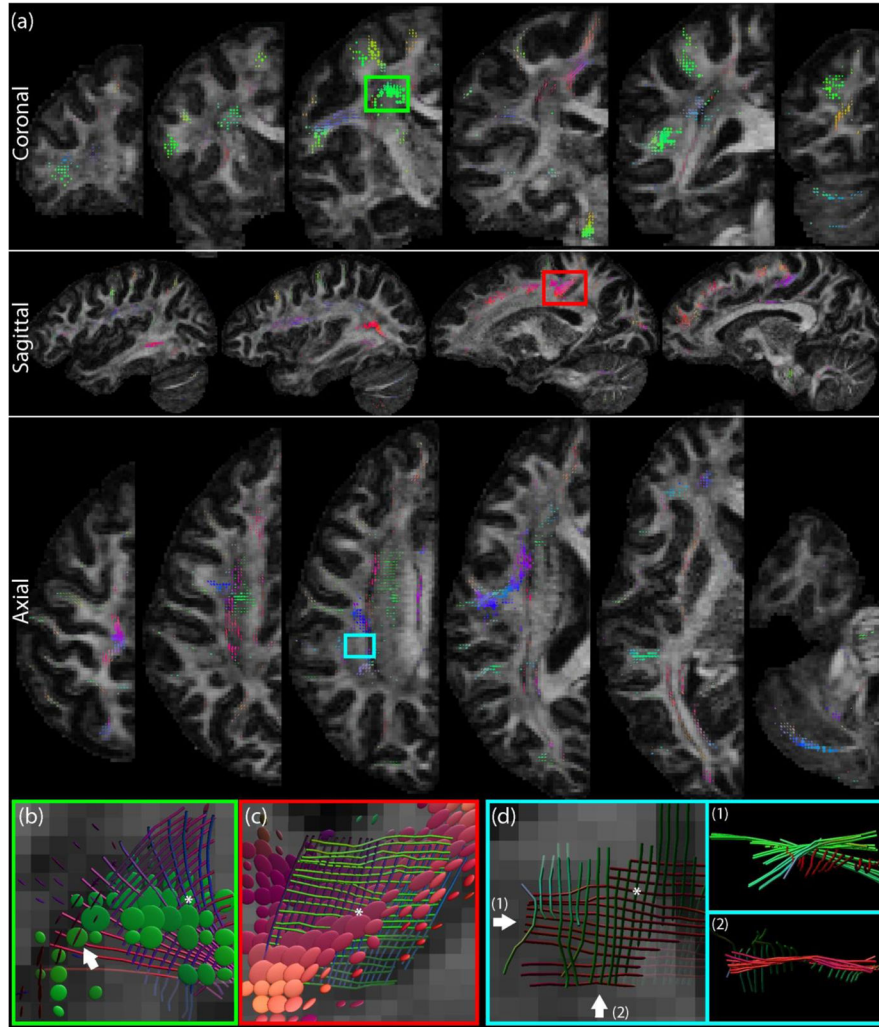


Fig. 12.

(a) Sheet tensors ($\lambda = 0.008$) on different coronal (top), sagittal (middle), and axial (bottom) slices. Ellipsoids with $P_\lambda < 0.2$ are not shown for clarity, and the sheet tensors are colored according to Fig. 5b. (b) High-SPI area with streamlines (paths $(\hat{\Phi}_{h_2}^W \circ \hat{\Phi}_{h_1}^V)(p)$ and $(\hat{\Phi}_{h_1}^V \circ \hat{\Phi}_{h_2}^W)(p)$ with $h_{max} = 5$ voxels used to compute the Lie bracket in a voxel marked by a white asterisk) of the CC and the CST in the left hemisphere. Non-orthogonal angles can be recognized, and the white arrow indicates crossing sheets. (c) A medial and sagittally oriented sheet structure, formed by parts of the CC/CST and anterior-posterior oriented association fibers. (d) A low SPI area in which the fibers look like a sheet from a superior view, but clearly diverge when inspecting other viewpoints (1) and (2).

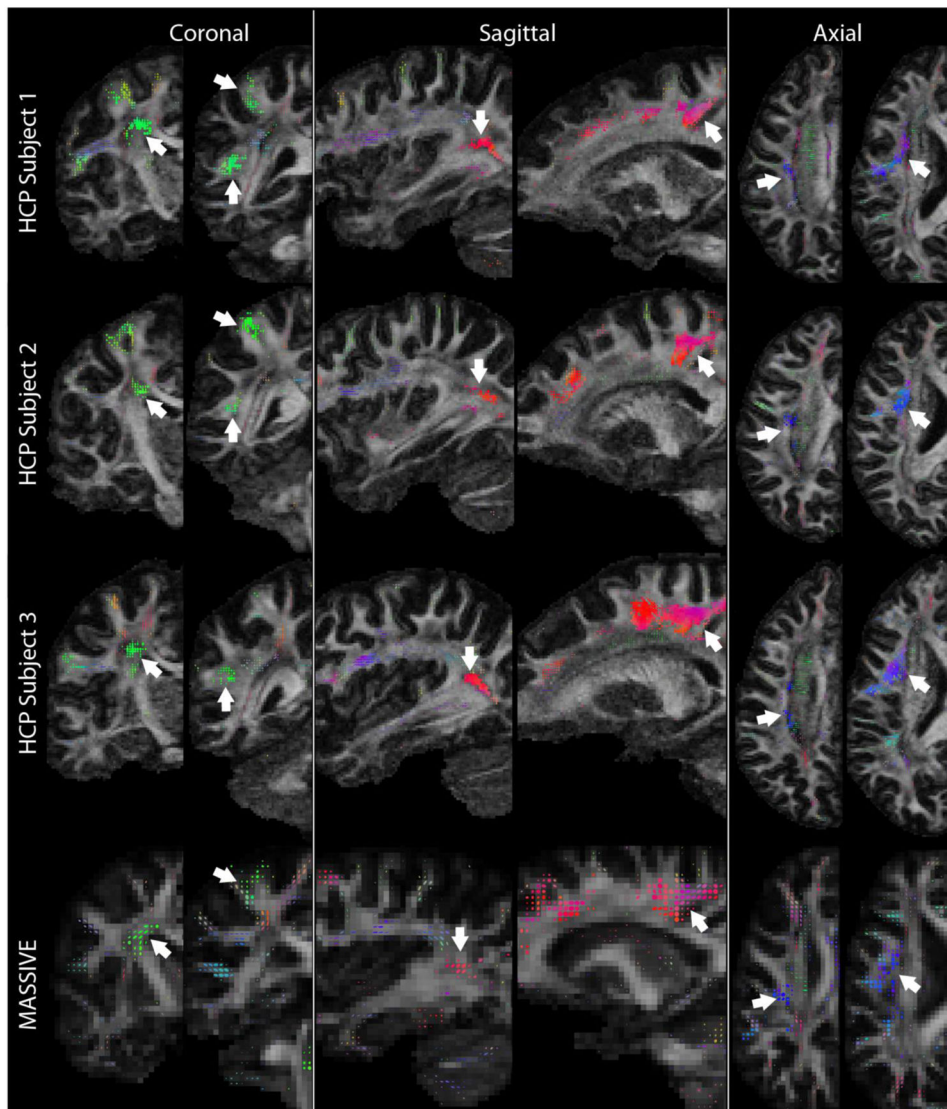


Fig. 13. Visual comparison of sheet structures between subjects and spatial scales (tensors with $P_\lambda < 0.2$ are not shown for clarity, colors according to Fig. 5b, and we set $\lambda = 0.008$). Examples of visually similar sheet structures are indicated by the arrows.

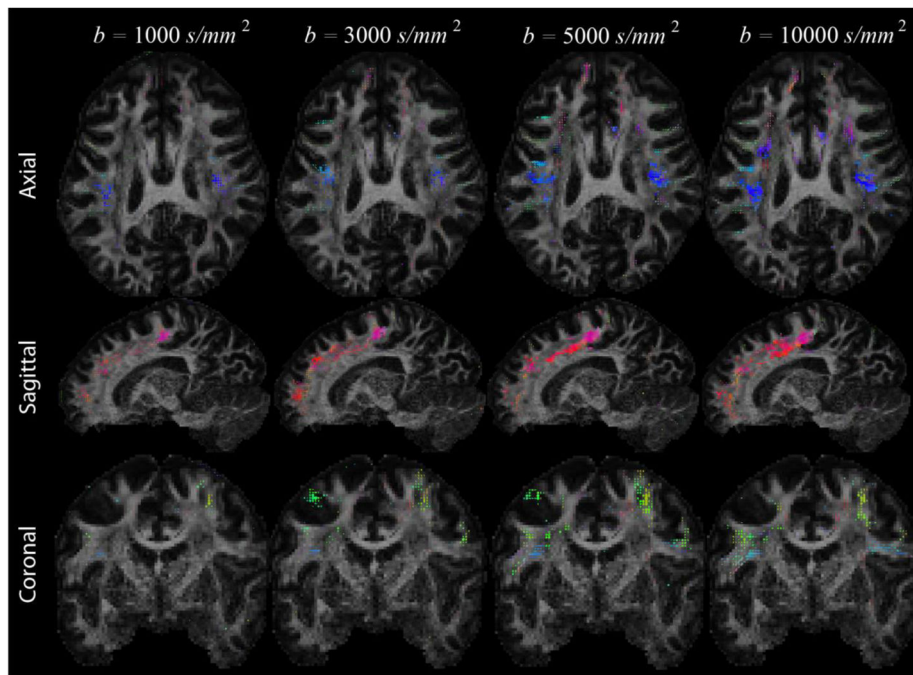


Fig. 14. The detection of sheet structure with different diffusion weightings in the MGH HCP data set, overlaid on the FA of the $b = 1000 \text{ s/mm}^2$ shell (tensors with $P_\lambda < 0.2$ are not shown for clarity, colors according to Fig. 5b, and we set $\lambda = 0.008$).

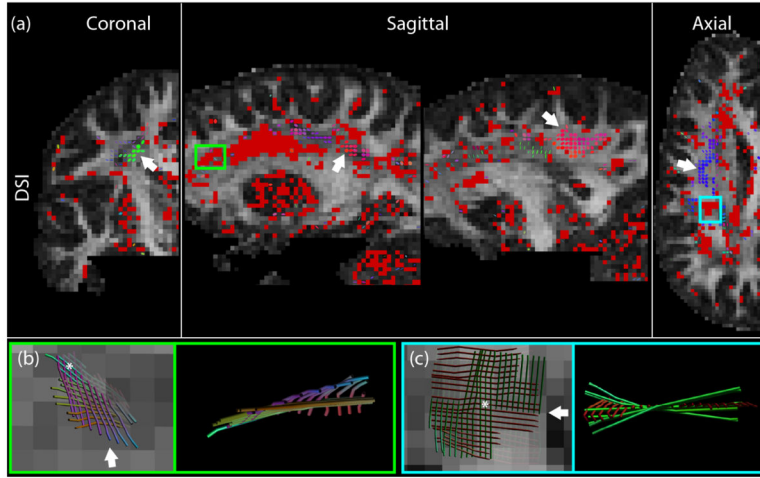


Fig. 15.

(a) A map of $\left| \left[\widehat{\cdot} \right]_p^\perp \right|$ for the MGH DSI dataset ($h_{max} = 3$). A tensor is visualized if $\left| \left[\widehat{\cdot} \right]_p^\perp \right| \leq 0.008$ with colors according to Fig. 5b (tensors have the same size, arrows indicate example areas), and we color the voxel red if the minimum $\left| \left[\widehat{\cdot} \right]_p^\perp \right|$ in that voxel is larger than 0.025. Rectangles show spatially continuous example areas of high minimal $\left| \left[\widehat{\cdot} \right]_p^\perp \right|$, the corresponding paths for the voxel marked by a white asterisk are visualized in (b) and (c). The pathways clearly do not form a sheet but instead ‘diverge’ from the plane when inspecting them from a rotated view (orientation indicated by arrows).